

Towards sector-based attribution using intra-city variations in satellite-based emission ratios between CO₂ and CO

Dien Wu¹, Junjie Liu^{2,1}, Paul O. Wennberg^{1,3}, Paul I. Palmer^{2,4}, Robert R. Nelson², Matthäus Kiel², and Annmarie Eldering²

¹Division of Geological and Planetary Sciences, California Institute of Technology, Pasadena, USA

²Jet Propulsion Laboratory, California Institute of Technology, Pasadena, USA

³Division of Engineering and Applied Science, California Institute of Technology, Pasadena, USA

⁴School of GeoSciences, University of Edinburgh, Edinburgh, UK

Correspondence: Dien Wu (dienwu@caltech.edu)

Abstract. Carbon dioxide (CO₂) and air pollutants such as carbon monoxide (CO) are co-emitted by many combustion sources. Previous efforts have combined satellite-based observations of multiple tracers to calculate their emission ratio (ER) for inferring combustion efficiency at regional to city scale. Very few studies have focused on ~~burning~~ combustion efficiency at the sub-city scale or related it to emission sectors using space-based observations. Several factors are important for deriving and interpreting spatially-resolved ERs from asynchronous satellite measurements including 1) variations in meteorological conditions ~~induced by different~~ given mismatch in satellite overpass times, 2) differences in vertical sensitivity of the retrievals (i.e., averaging kernel profiles), ~~and~~ 3) interferences from the biosphere and biomass burning, and 4) mismatch in the daytime variation of CO and CO₂ emissions. In this study, we extended an established emission estimate approach to arrive at spatially-resolved ERs based on retrieved column-averaged CO₂ (XCO₂) from the Snapshot Area Mapping (SAM) mode of the Orbiting Carbon Observatory-3 (OCO-3) and column-averaged CO from the Tropospheric Monitoring Instrument (TROPOMI).

To evaluate the influence of the confounding factors listed above and further explain ~~the~~ intra-urban variations in ERs, we leveraged a Lagrangian atmospheric transport model ~~and~~ with an urban land cover classification dataset and reported ER_{CO} from the sounding-level to the overpass- and city- ~~levels~~ level. We found that the difference in the overpass times and averaging kernels between OCO and TROPOMI strongly affect the estimated spatially-resolved ER_{CO}. Specifically, a time difference of > 3 hours typically led to dramatic changes in ~~the wind direction and shape of urban plumes~~ wind directions and urban plume shapes and thereby making the calculation of accurate sounding-specific ER_{CO} difficult. After removing ~~those such~~ cases from consideration and applying a simple plume shift method when necessary to account for changes in wind direction and speed, we discovered significant contrasts in combustion efficiencies between 1) two megacities versus two industry-oriented cities and 2) different regions within a city, based on six to seven nearly-coincident overpasses per city. Results suggest that ~~the combustion efficiency for heavy~~ ER_{CO} impacted by the industry in Los Angeles is slightly lower than ~~its the~~ overall city-wide value (< 10 ppb-CO / ppm-CO₂). In contrast, ERs-ER_{CO} related to the heavy industry in Shanghai ~~are found to be~~ is much higher than Shanghai's city-mean and more aligned with city-means of the two industry-oriented Chinese cities (approaching 20 ppb-CO / ppm-CO₂). Although investigations based on a larger number of satellite overpasses are needed, our ~~first analysis~~ unique approach (without using sector-specific information from emission inventories) provides

25 guidance for ~~estimating intra-city gradients in combustion efficiency from future~~ assessing combustion efficiency within a city
30 based on future satellite missions, such as those that will map column CO₂ and CO concentration simultaneously with high
spatiotemporal resolutions.

1 Introduction

Home to more than half of the total global population, urban areas have been expanding, especially ~~for in~~ Asia and Africa
30 with an urbanization rate of 1.3% and 1.1% yr⁻¹ between 2015 and 2020 (World Urbanization Prospects 2018). Urban regions
are also responsible for a significant amount of anthropogenic emissions of greenhouse gases (GHG) and air pollutants into
the atmosphere including carbon dioxide (CO₂), methane, carbon monoxide (CO), and nitrogen oxides (Duncan et al., 2016;
Lin et al., 2018; Super et al., 2017; Plant et al., 2019). To monitor the abundance of a number of atmospheric species in a
globally-consistent manner, satellite observations have become indispensable ~~in past years~~ (Yokota et al., 2009; Crisp et al.,
35 2012; Veeffkind et al., 2012). For example, carbon-monitoring satellites such as the Orbiting Carbon Observatory-2 (OCO-2,
Crisp et al., 2012) have made the quantification of city-scale CO₂ emissions and emission trends possible (e.g., Hedelius et al.,
2018; Ye et al., 2020; Wu et al., 2020; Shekhar et al., 2020; Lei et al., 2021). Quantifying the spatial gradient of atmospheric
concentrations and relating the gradient to emissions within the city domain becomes the next critical yet challenging task.
Understanding such spatial heterogeneity in emissions and the environmental consequences can support better decisions in
40 urban planning and pinpointing hotspots for emission mitigation.

~~To reduce emissions of greenhouse gases and air pollutants, targeting the efficiency during combustion activities~~ Given the
co-benefit between GHG reduction and improved air quality at various scales (Zhang et al., 2017), controlling the consumption
of fossil fuels altogether is the key. ~~Such efficiency~~ Efficiency associated with various combustion activities is linked to the
underlying ~~combustion~~ processes and conditions (e.g., oxygen-to-fuel ratio and temperature). For example, the amount of
45 CO₂ emitted from coal-fired power plants varies with thermal and pressure conditions, the type of fuel consumed, the tech-
nology deployed, and the service duration of power plants (Yuan and Smith, 2011). Modern power generation with distinct
scrubbing technology are often regarded as “clean” emitters leading to minimal CO and NO_x enhancements (Lindenmaier et al.,
2014). The commonly-used approach in estimating combustion efficiency is to combine atmospheric observations of multi-
ple trace gases ~~. Benefit from the cancellation of the errors in describing the atmospheric transport that carries tracers to the~~
50 ~~measurement site, the and report the~~ ratio of the total or excess measured concentrations (above a defined background value) be-
tween tracers ~~are reported (Silva and Arellano, 2017; Reuter et al., 2019; Park et al., 2021).~~ (Silva and Arellano, 2017; Reuter et al., 2019;
Such tracer-to-tracer ratio calculation has the benefit that errors in describing the atmospheric transport that carries tracers to
the measurement site can be cancelled. A few notable studies further utilized ~~their~~ derived emission ratios (ERs) from ground
or airborne measurements to infer sector-specific emission signals (Wennberg et al., 2012; Lindenmaier et al., 2014; Nathan
55 et al., 2018; Tang et al., 2020).

CO and NO_x often serve as tracers for anthropogenic CO₂ due to their ~~overlapping sources of combustion~~ common sources
(e.g., Palmer et al., 2006; Wunch et al., 2009; Hedelius et al., 2018). Analyzing remotely-sensed NO_x plumes with relatively

improvements and 2) between sub-sectors, e.g., gasoline vs. diesel vehicles or moving vs. congestion traffic (Westerdahl et al., 2009; Popa et al., 2014). Despite differences in measurement platforms and analyzing analysis approaches, the observed urban-integrated ER_{CO} values, especially for those in Europe and the United States, are well constrained within the range of 4 to 15 ppb ppm⁻¹ (**Fig. 1b**). ER_{CO} for biomass burning and shipping sectors are estimated based on fuel-specific emission factors, i.e., ER_{CO} (= EF_{CO} / EF_{CO₂}) with proper unit conversions, where emission factor EF_X indicates the emission of gas X per kg of fuel burned.

~~associated with specific processes (a) and integrated over the entire city/region (b) summarized from previous studies. X-axis indicates the time these estimates were made except for Akagi et al. (2011). 2011 was simply chosen for x-axis since the paper was published in 2011. The error bars represent the uncertainties in estimated ERs and transparent rectangle indicates the range of ERs over multiple years. Paper citations are omitted from the figure and included in Appendix A. ERs related to biomass burning and the shipping sectors are derived using emission factors of CO and. The range of the overpass-specific estimates for Shanghai, LA, Baotou, and Zibo derived from this work are also added to the figure (dashed black box).~~

~~The variability in observation-derived ERs among different combustion processes and sectors (**Fig. 1a**) hinders the generalization and representation of gridded ERs. Many~~ When estimating fossil fuel emissions from a bottom-up emission inventories simulate FFemissions using activity data for spatially allocating sector-based EFs perspective, most inventories rely on activity data and may involve prior knowledge of emission factors (Gurney et al., 2019; Solazzo et al., 2021). One notable example is Hestia, a high-resolution inventory for the US, which estimates CO₂ emissions of non-point sources based upon-up CO emissions from the National Emission Inventory ~~;~~ and-and-with EFs and carefully evaluates their adopted EFs (Gurney et al., 2019). However, ~~constructing inventories for the entire globe is data-demanding and challenging because accurate when constructing emission inventories across regions/nations, the large variability in ERs across combustion processes, sectors, years, and regions (as seen in Fig. 1a) makes the choice of EFs extremely challenging. Accurate~~ bottom-up ~~estimates require~~ emission estimates require accurate activity data and EF_X that naturally vary with combustion conditions (e.g., temperature, fuel load, oxygen level) and are generally not well known ~~;~~ especially over data-scarce regions. To our knowledge, only a few global inventories, such as the Emissions Database for Global Atmospheric Research (EDGAR, Solazzo et al., 2021), offer global anthropogenic CO and CO₂ emissions. Considering the challenge in approximating ERs, ~~the-certain~~ knowledge derived from atmospheric observations may 1) complement inventory-based ERs (e.g., CO:NO_x ratio in Lama et al., 2020) and 2) facilitate the emission constraint for a desired species, gas usually with relatively large-larger uncertainties (Wunch et al., 2009; Palmer et al., 2006; Wang et al., 2009; Brioude et al., 2012; Nathan et al., 2018). Such prior ~~success motivates us to derive ERs from achievements motivate us to examine ERs using~~ satellite observations of multiple tracers.

Most ~~previous studies have existing studies~~ focused on quantifying an integrated ER for the whole city or region. ~~As-We take~~ a step forward ~~;~~ we-to zoom into an urban area and leverage spatially-resolved satellite observations. Intra-city variations in the satellite-based concentration of a specific air pollutant like NO_x have been ~~examined-analyzed~~ and linked to societal inequality such-as-of-inequalities regarding the income and educational attainment (Demetillo et al., 2021; Kerr et al., 2021). Yet, no one has attempted to study the intra-urban gradient in combustion efficiency from space and ~~connect-such-relate such a~~ gradient to a specific combustion processsector. This is now possible by virtue of the Orbiting Carbon Observatory-3 (OCO-3) mounted

on the International Space Station (~~ISS~~) that can sample a city-landscape during ~~its~~ the Snapshot Area Mapping (SAM) mode
105 (Eldering et al., 2019; Taylor et al., 2020; Kiel et al., 2021). In ~~this~~ an effort to arrive at spatially-varying ERs from sensors
with asynchronous orbits, we must account for several factors that have not been thoroughly investigated. These include 1)
variations in meteorological conditions and emission patterns during different overpass times, 2) discrepancies in the vertical
sensitivity of the retrievals (i.e., averaging kernel or AK profiles), and 3) interference from non-anthropogenic sources and
sinks, especially from the biosphere.

110 ~~Motivated by the gaps in prior literature, we conducted an analysis to~~ In this study, we explore the spatial distribution of
ER_{CO} within four urban areas mainly using XCO₂ observations from OCO-3 and XCO observations from the TROPOspheric
Monitoring Instrument on board the Sentinel-5 Precursor (TROPOMI, ~~;~~ Veeffkind et al., 2012). To avoid relying on prior
~~sectoral information on~~ sector-specific information of ER_{CO} from emission inventories, we adopt the urban land cover data
from ~~the~~ high-resolution World Urban Database and Access Portal Tools (WUDAPT, ~~;~~ Ching et al., 2018). WUDAPT offers
115 the so-called Local Climate Zone (LCZ) that takes into account building structures of the building structure/spacing and along
with vegetation coverage (Stewart and Oke, 2012), which ~~can~~ shed light on ~~localized infrastructure within the city~~ the urban
infrastructure.

Our work seeks to answer the following two questions.

1. Is it possible to accurately quantify spatially-resolved ER_{CO} from asynchronous satellite measurements?
- 120 2. Can the combustion efficiency for a given sector be determined without using prior emission inventories?

~~In Section~~

In Sect. 2, we describe the satellite data and methodology for obtaining emissions, ER_{CO}, and associated uncertainties. In
~~Section Sect.~~ Sect. 3, we ~~present the results on~~ show intra-city variations in ER_{CO} (including ER_{CO} tied to heavy industry ~~areas~~ in a
megacity) and ~~its sensitivity to several interference factors~~. ~~In Section~~ how multiple factors may interfere in deriving ER_{CO}.
125 In Sect. 4, we discuss ~~the implication and limitation~~ implications and limitations of this analysis.

2 Data and methodology

We targeted two types of cities: 1) industry- and energy- oriented cities (Baotou, China and Zibo, China), and 2) megacities with
more diverse emission sectors (Shanghai, China and Los Angeles, US). The four cities are selected considering the amount and
quality of XCO₂ data from OCO-3 SAMs and TROPOMI XCO data. The two industry- and energy- oriented cities in China
130 are selected given their ~~considerable~~ large amount of metal production plants for aluminum or iron and steel (Global Energy
Infrastructure Emission Database, GID; Wang et al., 2019) and ~~surrounded~~ surrounding coal-fired power plants (Global Energy
Monitor, GEM; and the Global Power Plant Dataset; World Resources Institute, WRI, 2018) that support the nearby industries.

Our goal is to calculate ER_{CO} from every satellite sounding within an urban plume that is ~~the spatial extent a~~ downwind area
affected by urban emissions (**Sect. 2.2**). Sounding-dependent ER_{CO} are calculated as ratios of CO emissions over CO₂ emis-
135 sions (**Eq. 3**) that ~~estimated from the~~ are estimated from satellite-derived ~~FF~~ fossil fuel (FF) enhancements and further re-

140 fined with a “scaling factor” in Eq. 1. This scaling factor ~~is obtained from an atmospheric transport model (Sect. 2.2.1),~~
~~which~~ accounts for several mismatches between OCO-2/3 and TROPOMI (Sect. 2.1) ~~and is obtained from an atmospheric~~
~~transport model (Sect. 2.2.1). Since we do not differentiate emission signals due to biofuel or fossil fuel combustion, the~~
~~term “FF enhancement” is simply referred to as~~ *column enhancement induced by any anthropogenic combustion processes by*
145 *the target city*. Determination of FF enhancements requires an estimate of the background values (Sect. 2.2.2) and “second-
order” correction terms for biogenic and pyrogenic sources (~~see explanations in Sect. 2.2.3~~). ~~The sounding-specific ERs and~~
~~their Sounding-specific ERs and~~ uncertainties (Sect. 2.2.4) are aggregated to yield an ER per overpass and per city. ~~After~~
~~determining the intra-city variations in ER~~ Lastly, we illustrate how ~~much ERs~~ ER_{CO} associated with heavy industry in Los
Angeles and Shanghai can be extracted with the assistance of ~~the urban land cover classification dataset (WUDAPT, WUDAPT~~
145 ~~(Sect. 2.3)~~).

2.1 Satellite observations and data pre-processing

We ~~screened available data for overpass~~ evaluated all overpasses coincidences between OCO-3 SAM ~~X~~ and TROPOMI ~~X~~ CO
~~observations and TROPOMI observations but only selected those~~ with relatively small differences in overpass times. Consider-
ing the limited number of ~~the~~ coincidences between sensors, two non-SAM overpasses from OCO-3 and one OCO-2 overpass
150 are added to the analysis. ~~In the end, six to seven~~ As a result, six OCO-TROPOMI coincidences with higher data quality from
Oct 2019 to June 2021 were integrated into the final result for ~~each city. Only two every city. Two~~ of the total ~~25 overpasses~~
~~(both in June 2021)~~ 24 overpasses fall within the ~~north~~ northern hemispheric summer months ~~between June and August~~ (both in
June).

2.1.1 OCO-2/3 XCO_2

155 The column-averaged dry-air mole fraction of CO_2 (XCO_2) is retrieved from the reflected sunlight over two CO_2 bands
centered on 1.6 and 2.0 μm and the oxygen-A band for obtaining surface pressure ~~obtained by OCO-3~~ (Eldering et al., 2019;
Taylor et al., 2020). In addition to the standard Nadir, Glint, and Target modes, OCO-3 ~~performs SAMs that collect~~ collects
several adjacent swaths of XCO_2 observations over a spatial area of approximately 80 km by 80 km during its SAM mode,
e.g., four individual swaths in an overpass over LA on Feb 24, 2020 (Fig. 2a). Similar to OCO-2, each satellite swath is
160 comprised of eight spatial footprints/soundings and each sounding has an area of $\sim 1.6 \times 2.2$ km² at nadir (Fig. 2a). Our
analysis only used screened OCO-3 B10r/B10p4r data (Eldering, 2021) with an XCO_2 quality flag of zero (QF = 0). It is
worth highlighting ~~that~~ the B10r/B10p4r product is superior to the Early version ~~for of~~ OCO-3 (Taylor et al., 2020) including
improved ~~geolocation~~ geo-location, advanced radiometric calibration, improved quality filters, and customized post processing
bias correction. ~~Because~~ As OCO-3 is mounted on the ISS International Space Station that is in a precessing orbit, its overpass
165 time varies, for example, from 07:00 to 15:00 local time for the overpasses we examined, unlike OCO-2.

2.1.2 TROPOMI XCO

The [TROPOMI](#) column density of CO molecules [mole cm^{-2}] is retrieved via the measured radiation from the shortwave infrared wavebands [on TROPOMI](#), centered at $\sim 2.3 \mu\text{m}$ (Veefkind et al., 2012). We ~~only selected data~~ [selected soundings](#) with quality assurance ≥ 0.5 [as](#) recommended by the TROPOMI ~~readme~~ [README](#) document (Landgraf et al., 2020) and converted the column density to the total column-averaged dry-air mole fraction of CO [[XCO in ppb](#)] [using by calculating the](#) dry-air column density [mole cm^{-2}] ~~estimated~~ from retrieved surface pressure and total column water vapor. TROPOMI CO is retrieved at a larger pixel area of $\sim 7 \times 7 \text{ km}^2$ at Nadir and reduced to $5.5 \times 7 \text{ km}^2$ after Oct 6, 2019 (**Fig. 2c**). The overpass time of TROPOMI is $\sim 13:30$ local time of equatorial overpass for nadir measurements with a time span of 1–2 hours for soundings on the edge of its wide swath (i.e., $\sim 2600 \text{ km}$).

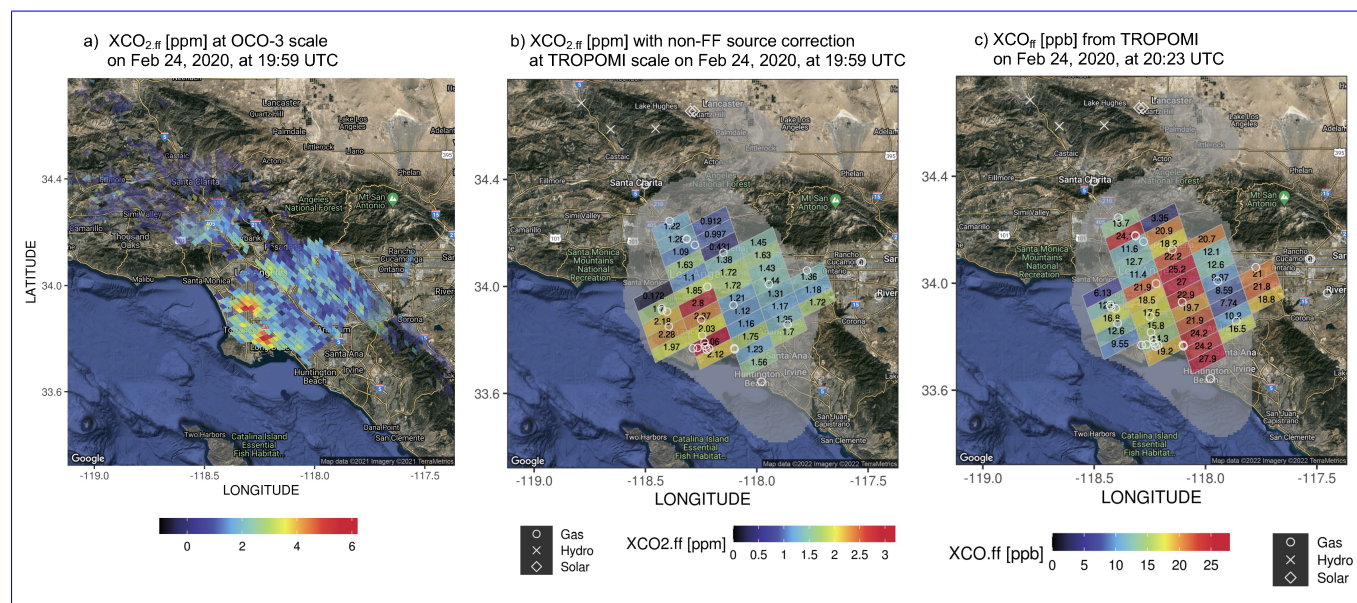


Figure 2. [Spatial maps of FF XCO₂ enhancements with corrections of non-FF sources at native OCO-3 scale \(a, ppm\) and aggregated at the TROPOMI scale \(b, ppm\) along with FF XCO enhancements \(c, ppb\) over Los Angeles on Feb 24, 2020.](#) Power stations with different primary fuel types are displayed in different white symbols based on the Global Power Plant Dataset (World Resources Institute, 2018). The overall X-STILT column footprint [$\text{ppm} / (\mu\text{mol m}^{-2} \text{ s}^{-1})$] from all soundings is drawn in light grey (see explanations for column footprint in [Sect. 2.2.1](#)). The underlying hybrid maps were created using the ggmap library in R with the hybrid view of Google Maps over LA (copyright: Map data ©2021 Imagery ©2021 TerraMetrics).

175 2.1.3 Differences between two sensors/species

Four mismatches between OCO-3 XCO₂ and TROPOMI XCO pose challenges in extracting FF enhancements and ER_{CO} from atmospheric observations, which ~~we attempt to account for and assess~~ [are accounted for in this analysis](#):

1. [Satellite pixel area: We searched for XCO₂ enhancements from multiple OCO-2/3 soundings falling within each TROPOMI polygon and averaged the corresponding enhancements to the TROPOMI scale a given TROPOMI polygon are grouped](#)

180 and averaged (Fig. 2a vs. b). For simplicity, ~~we used~~ the centered lat/lon coordinate of an OCO-3 sounding OCO pixel
is used to determine its corresponding TROPOMI polygon. ~~Retrieval uncertainties and observation noise (defined as the~~
~~variability within each TROPOMI polygon) are estimated at the TROPOMI pixel scale and propagated as part of the total~~
~~observed~~ The retrieval uncertainty tied to each OCO sounding is also aggregated according to the TROPOMI sampling,
contributing to the total observational uncertainty (Sect. 2.2.4).

185 2. *Averaging kernel profile*: Within the planetary boundary layer where most emissions occur, TROPOMI XCO retrieval is
affected by cloud height/fractions, which yields lower-than-unity AK (**Supplementary Fig. ??**). OCO-2/3 XCO₂ under
cloudy conditions are typically omitted from Lite files and when QF = 0 is applied; thus, its AK normally approaches
one near the surface for cloud-free scenes. The mismatch in AKs between sensors must be accounted for as it can affect
the interpretation of ERs. In this work, we accounted for AK-AKs within an atmospheric transport model (Sect. 2.2.1).

190 3. *Overpass ~~time and upwind times~~, meteorological ~~condition~~conditions, and emission variations*: As a result of the
~~sometimes large time difference~~, ~~meteorological conditions including the overpass time difference between sensors,~~
~~variations in meteorological conditions (e.g., wind direction and speed can change significantly, leading)~~ can lead to
changes in urban plume shapes detected by the two sensors as they pass by. We dealt with changes in wind speed and
wind direction separately. The former is resolved by the “scaling factor” ~~generated from the~~ inferred from an atmospheric
195 transport model and the latter undergoes manual evaluations (Sect. 3.1). Besides, CO and CO₂ emissions themselves
can vary over the course of a day, e.g., driven by road transportation and residential sectors. Given the overpass time
difference between sensors, it is likely that such mismatch in the timing of CO versus CO₂ emissions may affect the
observed ER_{CO}.

200 4. *Non-fossil fuel sources/sinks*: The lack of account of influence from the biosphere and biomass burning may ~~affect~~
~~the calculation of bias~~ ER_{CO}. Given our definition of ~~background regions~~ a local background, the contrast in non-FF
concentration anomalies between the urban and ~~background region may interfere the calculation of FF enhancements~~
~~and (more explanations in the background region needs to be included (for more explanation, see Sect. 2.2.3).~~

205 ~~FF enhancements at the native OCO-3 soundings (a, ppm) and aggregated to the TROPOMI scale (b, ppm), and XCO~~
~~enhancements (c, ppb) over Los Angeles on Feb 24, 2020. Power stations with different primary fuel types are displayed in~~
~~different white symbols based on the Global Power Plant Dataset (World Resources Institute, 2018). The X-STILT column~~
~~footprint from all soundings are drawn in light grey (see explanations for column footprint in Sect. 2.2.1). The underlying~~
~~hybrid maps were created using ggmap library in R that adopted the Google Maps (copyright: Map data ©2021 Imagery~~
~~©2021 TerraMetrics).~~

2.2 Estimates of E_{gas}, ER_{CO} and uncertainties

210 Previous studies (Mitchell et al., 2018; Wu et al., 2020; Lin et al., 2021) proposed an approach to calculate ~~the an~~ overall
CO₂ or CH₄ ~~fluxes~~ flux using atmospheric measurements and atmospheric transport model ~~without~~, without relying on prior

information from emission inventories. Here we briefly describe this approach to obtain the overall emission of either CO₂ (Eq. 1) or CO (Eq. 2) for ~~each sounding~~ a single sounding S, modified from Wu et al. (2020):

$$\langle E_{CO_2,s} \rangle = \frac{X_{ffCO_2,s}}{\langle XF_{CO_2,s} \rangle} = \frac{X_{obsCO_2,s} - X_{bgCO_2} - \delta X_{bioCO_2,s} - \delta X_{bbCO_2,s}}{\iint XF_{CO_2,s}(x,y) dx dy} \quad (1)$$

$$215 \quad \langle E_{CO,s} \rangle = \frac{X_{ffCO,s}}{\langle XF_{CO,s} \rangle} = \frac{X_{obsCO,s} - X_{bgCO} - \delta X_{bbCO,s}}{\iint XF_{CO,s}(x,y) dx dy} \quad (2)$$

All the X terms in the numerator contribute to ~~FF~~ the estimate of FF column enhancements (X_{ff} , Fig. 2). ~~In theory,~~ X_{ff} at a downwind satellite sounding S is the sum of its corresponding S is the net result of FF sources over ~~its corresponding the~~ source region (x, y) . To describe ~~and attribute this source region~~ the source region and attribute it to each satellite sounding, we adopted the column version of the Stochastic Time-Inverted Lagrangian Transport (X-STILT) model (Lin et al., 2003; Fasoli et al., 2018; Wu et al., 2018). ~~Using X-STILT, we can~~ From this model, we obtain a “scaling factor” $\langle XF_{gas} \rangle$ ~~that accounts for~~ to account for the sounding-specific AK profile and meteorology (Sect. 2.2.1).

~~Within the calculation of FF enhancements of either or XCO₂,~~ X_{bg} ~~represents the background values calculated from~~ denotes the local background values using satellite observations uncontaminated by the ~~urban plume city emission~~, which are ~~normally~~ constant for a group of ~~observations (i. e., not sounding-specific, background observations. The background region is usually~~ chosen over rural region outside the urban plume with consideration of wind direction (Sect. 2.2.2). ~~The~~ From a Lagrangian viewpoint, the air parcels arriving at ~~the sounding in the city center can have different origins and pathways~~ an urban sounding might be traced back to different origins from the air parcels ~~that arrived at~~ arriving at a rural sounding. ~~These,~~ meaning observations at the two soundings may be influenced differently by ~~biospheric fluxes and biomass burning emissions~~ the surrounding biosphere. Hence, two background correction δ -terms are attached to ~~correct account~~ for the urban-background gradient in ~~column~~ anomalies from the concentration anomalies due to net ecosystem exchange (NEE) and biomass burning (Sect. 2.2.3 ~~and~~ Eq. 4).

~~Similar to, the resultant~~ For a given sounding, the estimated flux $\langle E_{gas} \rangle$ with unit of $\mu\text{mol m}^{-2} \text{s}^{-1}$ ~~is tied to each sounding. These fluxes represent the total emissions in the source region with respect to a given TROPOMI sounding and represents the average emission over the corresponding source region of that sounding, which~~ should not be confused with the direct emission at that sounding location. The ER_{CO} for a given sounding S is then derived from Eqs. 1 ~~and~~ & 2 as follows:

$$ER_{CO,CO_2,s} = \frac{\langle E_{CO} \rangle}{\langle E_{CO_2} \rangle} \frac{\langle E_{CO,s} \rangle}{\langle E_{CO_2,s} \rangle} = \frac{X_{ffCO}}{X_{ffCO_2}} \frac{\langle XF_{CO} \rangle}{\langle XF_{CO_2} \rangle} \frac{X_{ffCO,s}}{X_{ffCO_2,s}} \frac{\langle XF_{CO,s} \rangle}{\langle XF_{CO_2,s} \rangle} = \frac{X_{ffCO}}{X_{ffCO_2}} \frac{X_{ffCO,s}}{X_{ffCO_2,s}} \gamma_{foot,foot,s} \quad (3)$$

~~$\frac{X_{ffCO}}{X_{ffCO_2}}$ is the~~ where ~~$\frac{X_{ffCO,s}}{X_{ffCO_2,s}}$ is the~~ observed enhancement ratio and ~~γ_{foot} informs~~ $\gamma_{foot,s}$ measures how enhancement ratios without ~~accounting for~~ considering AKs and meteorology differ from emission ratios. We simply use ppb-CO/ppm-CO₂ for units of ER_{CO} (same as mmol-CO/mol-CO₂).

240 2.2.1 The X-STILT model

The X-STILT model is adopted ~~for three purposes: to in this study,~~ 1) to provide the scaling factor $\langle XF_{\text{gas}} \rangle$ that resolves ~~the influences from differences in AK and wind fields between sensors~~ differences in AKs and changes in wind speeds; 2) ~~identify the to identify an~~ overpass-specific urban plume for ~~background determination~~ determining background regions (Sect. 2.2.2); ~~and to;~~ and 3) ~~estimate the sounding-level to estimate the sounding-specific~~ biogenic and pyrogenic ~~contributions to the~~ background anomalies for background corrections (Sect. 2.2.3).

STILT releases an ensemble of air parcels from target observations (known as the STILT “receptor”) and tracks the movement of those air parcels backward in time. The source region corresponding ~~for to~~ each sounding is informed by the “source-receptor relation” or the STILT “footprint” (Lin et al., 2003; Fasoli et al., 2018). The STILT footprint [ppm / ($\mu\text{mol m}^{-2} \text{s}^{-1}$)] describes the change in atmospheric concentration [ppm] at a downwind location due to possible upwind sources/sinks [$\mu\text{mol m}^{-2} \text{s}^{-1}$].

250 The magnitude of STILT footprints ~~tend tends~~ to be higher close to the target ~~observations observation~~ or under steadier wind ~~condition, as conditions, thus,~~ air parcels within the boundary layer can interact more ~~closely~~ with fluxes from the surface.

To accommodate the use of satellite-based column data, X-STILT incorporates ~~the~~ retrieval-specific AK and pressure weighting (~~PW~~) ~~profiles in profiles to~~ the footprint calculation (Wu et al., 2018), such that the influence ~~of on~~ air parcels originating from various altitudes of an atmospheric column are weighted by ~~the~~ sounding- and sensor- specific ~~AK vertical~~ profile

255 (Supplementary Fig. ??). The “column footprint” ~~;(XF_{gas}, becomes)~~ measures the sensitivity of the total column concentration to upwind fluxes ~~;-Because AK profile is specific to the retrieval from the perspective of a specific satellite sensor. For instance,~~ XF_{gas} for TROPOMI XCO differs from ~~that~~ XF_{gas} for OCO-2/3 XCO₂ even for concurrent observations (Eqs. 2, 1). ~~Because;~~ ~~Since~~ the air flow arriving at each satellite observation is unique, the magnitude and spatial distribution of ~~column~~ footprints ~~vary from one sounding to another~~ XF_{gas} ~~vary across soundings~~ (Supplementary Fig. ??). ~~If By~~ taking an average

260 of these sounding-dependent column footprints, as shown in Supplementary Fig. ??, we can identify the source region for all soundings in a SAM ~~as indicated by the~~ (light gray area in Fig. 2b,c). In this work, we only traced air parcels ~~back~~ for 12 hours ~~backward in time for calculating to calculate~~ column footprints, which is sufficient to capture the near-field influence from the target city ~~and better aligned with the local background region outside the city~~ (Sect. 2.2.2).

In ~~summary short,~~ the spatial summation of column footprints $\langle XF_{\text{gas}} \rangle$ is regarded as a scaling factor ~~in addressing the~~ ~~sensor specific to address the sounding specific~~ meteorological condition and AK profile. The ~~deviation of the~~ term γ_{foot} ~~in Eq. 3 from 1 as derived from Eq. 3~~ reveals the difference between a simple ~~concentration~~ enhancement ratio and a more robust, model-corrected emission ratio.

2.2.2 Background definition X_{bg}

Defining accurate background levels to extract urban FF enhancements has always been a challenge in top-down analysis,

270 especially when dealing with column measurements with small signal-to-noise ratio. Wu et al. (2018) compared several approaches to determine ~~the a~~ localized XCO₂ background for extracting urban signals from OCO-2, including approaches that

- 1) solely use satellite observations with statistics ~~like percentile or median~~ (e.g., ~~daily median~~);
- 2) solely use ~~atmospheric~~

~~transport models~~ an atmospheric transport model (e.g., ~~curtain method and the “curtain method”~~ based on global concentration fields); and 3) ~~combines observations and model. The latter two methods do not involve prior information on emissions~~ combine observations and transport information from models. Here, we expand the third approach to arrive at localized swath-dependent ~~XCO₂ and~~ background values. The broader spatial coverage and multiple swaths ~~of~~ stretching out of the city domain of OCO-3 SAMs ~~improve the determination of the background terms~~ help improve such background determination by introducing spatial variations in the background, compared to the narrow swath of OCO-2. Accurately describing ~~the latitudinal or~~ spatial gradients in background XCO₂ ~~have been emphasized previously~~ has been emphasized recently (Ye et al., 2020; Schuh et al., 2021).

The process of background determination used in this work involves a first step of identifying the urban plume and differentiating soundings as within or outside of the plume. ~~Here we used~~ To outline the urban plume shape at the overpass time, we utilized the forward mode of STILT with the inclusion of wind uncertainty ~~to~~ into atmospheric dispersion. Specifically, 1000 air parcels were released continuously from a rectangle representing the ~~urban extent~~ city domain (dashed black box in **Fig. 3**) every 30 minutes starting from 10 hours ahead of the overpass time. All air parcels are allowed to travel forward in time for 12 hours from their initial release ~~times~~ times. A random wind component typifying model-data wind errors is added to the parcel dispersion (Lin and Gerbig, 2005). We subset the air parcels only during the overpass time and applied a 2-dimensional kernel density estimate (KDE) based on ~~the~~ parcels' spatial ~~distribution~~ distributions (blue to purple contours in **Fig. 3**). KDE is carried out using the kde2d function provided by the MASS library in R (Venables and Ripley, 2002). These normalized KDE contours ~~then denote~~ indicate the likelihood and shape of an urban plume when the satellite scans through. The extent of the urban plume is finalized using a normalized KDE contour of 0.15 (black curve in **Fig. 3**), which is proper to 1) include soundings with possible influence from the target city and 2) exclude observations elevated by another city (e.g., ~~the~~ red polygons centered at ~~around~~ ~32°N and 120°E in **Fig. 3c**). This procedure is carried out separately for OCO-2/3 and TROPOMI to ~~address differences in the urban plume~~ reveal the impact of changing meteorology on urban plumes at different overpass times (see **Sect. 3.1**). It is worth stressing that only enhancements within the urban plume are ~~selected to yield~~ used for ER_{CO} estimates.

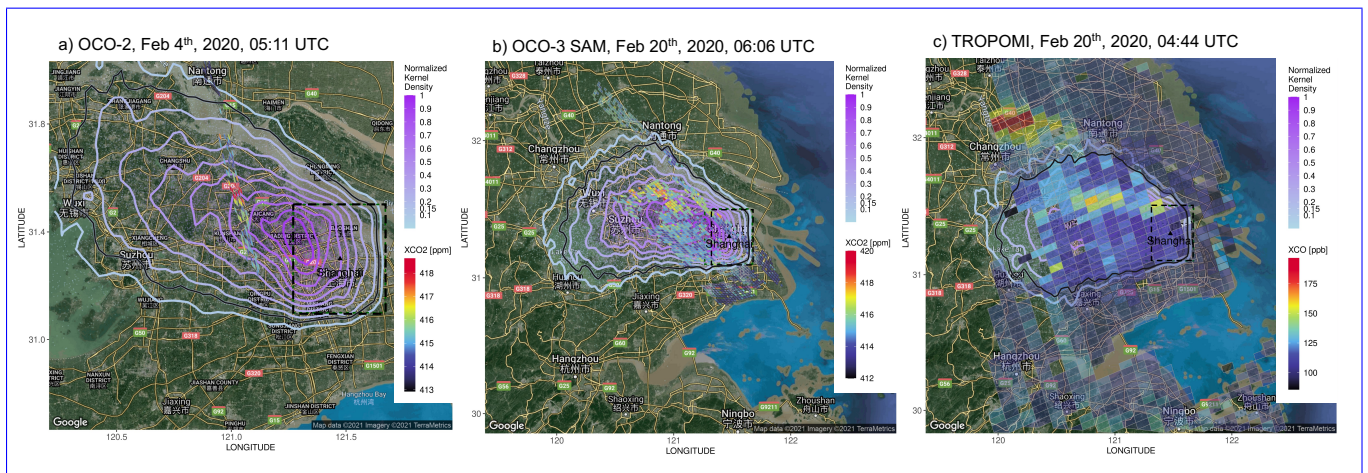


Figure 3. Demonstrations of background determination from OCO-2 XCO₂ on Feb 4, 2020 (a), OCO-3 SAM XCO₂ [ppm] and TROPOMI XCO [ppb] on Feb 20, 2020 (b, c) over Shanghai. The model-based urban plume (solid black curve) is determined by the normalized 2-D kernel density of the air parcels' distribution during the overpass time (blue-purple contours). The "background soundings" outside the urban plume are highlighted with black outlines, while other soundings are outlined in white. For example, OCO-2 observations to the north outside the plume (~121.1°E, 31.9°N, a) and OCO-3 and TROPOMI soundings to the southeast outside the plume (b, c) are used to estimate background values and background uncertainties. The underlying hybrid maps were created using the gmap library in R with the hybrid view of Google Maps over Shanghai (copyright: Map data ©2021 Imagery ©2021 TerraMetrics).

Next, the background value is calculated as the median value of observed X_{gas} per swath over the background region. For example, the background region is the area to the east outside the urban plume since southeasterly wind dominates (**Fig. 3b,c**). Background values vary with swaths if an OCO-3 SAM is examined. We chose the median instead of the mean to minimize the impact of any "outliers" that may be from a second FF source (other than our target cities) in the background region. **When analyzing data from OCO-2's narrow swath (Fig. 3a), the latitude range outside the plume serves as the background region and can be sensitive to the modeled wind bias and number of valid soundings (Wu et al., 2018). Fortunately, modeled wind bias is generally less of an issue when analyzing SAMs, because the broader coverage of valid SAM observations helps evaluate model-based urban plumes. Background uncertainties are estimated and propagated into the ER Background uncertainty is estimated as a component of the total observed uncertainty (Sect. 2.2.4).**

Demonstrations of background determination from OCO-2 on Feb 4, 2020 (a), OCO-3 SAM ppm and TROPOMI XCO ppb on Feb 20, 2020 (b, c) over Shanghai. The model-based urban plume (solid black curve) is determined by the normalized 2-D kernel density of the air parcels' distribution during the overpass time (blue-purple contours). On Feb 20, 2020, measurements to the east outside modeled plumes are identified as the "background measurements". The underlying maps were created using gmap library in R that adopted the Google Maps (copyright: Map data ©2021 Imagery ©2021 TerraMetrics).

2.2.3 Background correction terms for non-FF sources/sinks

The swath-dependent local background approach described above explicitly assumes equal contributions from non-FF sources and sinks for soundings in the background versus soundings in the urban plume. ~~We further estimated urban-background gradients in resulting~~, which may not always be the case. We then correct for the spatial gradient in contributions from biogenic and pyrogenic fluxes.

As ~~initially~~ proposed in Wu et al. (2021), rather than ~~the absolute biogenic or pyrogenic~~ absolute biogenic concentration anomalies, it is the contrast in these anomalies between the background versus ~~urban region~~ the urban plume that is required, ~~given our considering our localized~~ background definition. Specifically, hourly ~~column footprints from X-STILT~~ X-STILT column footprints are convolved respectively with hourly mean NEE from a biogenic biospheric model representation and ~~the~~ daily mean wildfire emissions from the Global Fire Assimilation System (GFAS, Kaiser et al., 2012) to estimate the sounding-specific absolute column anomalies X_{bio} and X_{bb} ~~for every sounding~~. The Solar-Induced Fluorescence (SIF) for Modeling Urban biogenic Fluxes (SMUrF, Wu et al., 2021) model estimates gross primary production (GPP) from a Contiguous SIF product (CSIF trained based on OCO-2 SIF, Zhang et al., 2018) and respiration based on modeled SIF-based GPP, air and soil temperatures.

Next, the urban-background gradient in ~~the anomalies are~~ such anomalies is calculated as the difference between ~~the~~ sounding-specific anomalies and the ~~average anomalies over~~ mean anomaly within the background region:

$$\delta X_{\text{bioCO}_2}(s) = X_{\text{bioCO}_2}(s) - \overline{X_{\text{bioCO}_2}(s_{\text{bg}})} \quad (4)$$

where s or s_{bg} represents all the soundings or ~~selected~~ select soundings in the background region, respectively. Let us imagine a north hemispheric summer day at noon, ~~when in the north hemisphere~~, the urban core is normally associated with a weaker biospheric uptake than the surrounding rural region, ~~biogenic~~. Biogenic signals $X_{\text{bioCO}_2}(s)$ for soundings in the city are less negative than the mean biogenic signal over the rural background $\overline{X_{\text{bioCO}_2}(s_{\text{bg}})}$. Hence, the urban-background biogenic gradient $\delta X_{\text{bioCO}_2}(s)$ is normally positive and ~~should~~ be subtracted from the ~~observed column to yield the FF enhancement total column~~ (Eq. 1). ~~Modeled sounding-specific~~ Estimated X_{bio} , ~~the and their~~ urban-background gradient δX_{bio} , ~~and their impacts on are discussed~~ are shown in Sect. 3.1.

Flux exchanges from the ocean and chemical transformation (e.g., CO sink via hydroxyl radical (OH) and source from oxidation of volatile organic compounds, VOCs) are not considered. The average lifetime of CO against OH ~~lasts for ranges from~~ a few weeks to several months depending on the season, much longer than the few-hour timescale we care about. Yet, CO can be generated from the oxidation of CH_4 and non-methane VOCs at various rates, which ~~are discussed in~~ is discussed in Sect. 4.4.3.

2.2.4 ~~uncertainty~~ Uncertainty sources

The uncertainty related to emissions should contain uncertainties from 1) the atmospheric transport (i.e., column footprints), 2) ~~the retrieval and measurement~~ observations, and 3) ~~background, and~~ 4) ~~non-FF~~ gradients. However, we sources and sinks,

according to Eqs. 1 or 2. We neglect uncertainties from column footprints ~~by assuming no systematic transport bias associated with the X-STILT simulations during OCO and TROPOMI overpass times~~ assuming no transport bias exists during either OCO or TROPOMI overpass time. The urban-background gradient in non-FF fluxes remains very small compared to FF enhancements (Sect. 3.1).

Observed uncertainty of We estimated uncertainties of observed FF enhancements following Eq. 5. As previously described, observations from a few screened OCO soundings (~ 5 to 28 OCO soundings depending on the TROPOMI footprint size) are averaged to arrive at mean XCO₂ ~~are comprised of retrieval errors and measurement noise (or at the TROPOMI scale. Due to such averaging/binning process, the XCO₂ variability) as the uncertainty due to binning is considered using the standard deviation of XCO₂ observations ($\sigma_{\varepsilon,bin}^2$ in Eq. 5) within a TROPOMI polygon. Depending on the TROPOMI sounding size (nadir or not) and the amount of screened OCO-3 soundings, there could be 5 to 28 OCO-3 soundings per TROPOMI polygon~~

$$\sigma_{\varepsilon,obs}^2 = \sigma_{\varepsilon,bin}^2 + \sigma_{\varepsilon,bg}^2 + \sigma_{\varepsilon,retrov}^2 \quad (5)$$

$\sigma_{\varepsilon,bin}^2$ is not required for estimating XCO uncertainty. Background uncertainty ~~contains ($\sigma_{\varepsilon,bg}^2$) contains both~~ the retrieval error and the ~~measurement noise of observations over~~ variability of column observations (as standard deviation) within background regions. ~~Retrieval errors associated with each OCO-3 sounding are aggregated to the~~

The retrieval uncertainty ($\sigma_{\varepsilon,retrov}^2$) of XCO is available for each TROPOMI sounding, whereas that of XCO₂ is reported for individual OCO-2/3 sounding (as read from Level 2 Lite files), which need to be aggregated at the TROPOMI scale. Due to possible correlations in retrieval errors between nearby OCO soundings, we estimated the error correlation length scale (L_x) using exponential variograms as demonstrated in Supplementary Fig. ???. Within a TROPOMI ~~spatial scale in a standard deviation of mean manner. Hence, polygon that contains N numbers of OCO soundings, an error variance-covariance matrix with a dimension of $N \times N$ is constructed with its diagonal elements filled with OCO sounding-specific retrieval error variance. Then, L_x is used to form the normalized covariance matrix, i.e., $exp(-\frac{D(S_i, S_j)}{L_x})$ where $D(S_i, S_j)$ denotes the distance between each two OCO soundings ($1 \leq i < j \leq N$). Lastly, the fewer OCO-3 soundings in a given TROPOMI polygon, the larger the observed uncertainties will be, which accounts for the unequal OCO-3 sampling in a TROPOMI polygon.~~ sum of all elements in the error covariance matrix (both variance and covariance elements) is divided by N^2 to obtain one $\sigma_{\varepsilon,retrov}^2$ per TROPOMI grid. As a result, the overall uncertainty of FF enhancement per sounding is often predominated by the background error component.

2.3 Identifying ER_{CO} for heavy industry within a city

One A key objective of our this study is to explain the intra-city variability of ER_{CO} by exploring the sector-specific or sector-dominant ~~burning combustion~~ activities. While certain combustion processes and sectors tend to have higher ERs than others, the sectoral-dependent ER are likely variable within and across cities. ~~Moreover, the ERs determined~~ The ERs derived from atmospheric observations comprise a mixed effect of different ~~sectoral activities~~ activities in the city. Previous attempts

include reducing the number of sectors and relying on prior ~~knowledge of~~ sector-specific ERs ~~in via~~ a (joint) Bayesian inversion
375 ~~(Nathan et al., 2018; Brioude et al., 2012)(Brioude et al., 2012; Nathan et al., 2018).~~

~~Map of Local Climate Zone (LCZ) from WUDAPT at a grid spacing of 120 m (a and d with zoomed-in images on b and
e) and interpolated areal coverage of heavy industry % at 1 km around Shanghai and Los Angeles (c, f). LCZ classifications
centered on Wuxi and Shanghai are combined. Power stations based on the Global Power Plant Dataset (World Resources
Institute, 2018) are drawn on the map as different symbols. The lightgray and white dashed rectangles in the first and third
380 columns indicate the zoomed-in region of the second column.~~

Here, we propose ~~a novel approach~~ to identify ERs associated with ~~heavy industry within the heavy industry in~~ a city. Instead
of relying on prior emission inventories that can sometimes be erroneous regarding the magnitude and ~~location of sectoral the~~
~~location of sector-specific~~ activities (see discussions in **Sect. 4.4**), we ~~utilize a~~ ~~utilized an~~ urban land cover classification
dataset. ~~The World Urban Database and Access Portal Tools (WUDAPT, Fig. 4a, d) project.~~ ~~WUDAPT that~~ provides Local
385 Climate Zone (LCZ) classifications at a grid spacing of 120 m (Ching et al., 2018). ~~Example As shown in Fig. 4a, d.~~ LCZ
categories include street canyons (e.g., compact/open/lightweight, high-/mid-/low-rise), building spacing (e.g., sparsely built,
heavy industry), and tree spacing (e.g., ~~e.g.,~~ dense/scattered trees, low plants, rocks, etc) ~~(Stewart and Oke, 2012)~~. Each LCZ is
unique in its thermal, radiative, and metabolic properties. For instance, compact high-rise (LCZ 1) and heavy industry (LCZ
10) categories have the highest anthropogenic heat output of 50–300 W m⁻² and > 300 W m⁻², respectively (Stewart and
390 Oke, 2012). Heavy industry is defined as low-rise and mid-rise industrial structures (towers, tanks, stacks) and mostly paved
or hard-packed metal with steel and concrete construction materials with few or no trees ~~in WUDAPT~~ (Ching et al., 2018),
which differs from the industry-relevant sectors ~~(e.g., from defined by~~ the Intergovernmental Panel on Climate Change ~~).~~ ~~Some~~
~~industries are also found within the WUDAPT-based heavy industry region (Figure 4 (e.g., as used in EDGAR)).~~ We clarify that
we are not trying to tackle individual industrial processes, ~~but treat some as an entity according to land cover data. Note that~~
395 ~~WUDAPT which is much more difficult.~~ LCZ maps are only available for a limited number of cities ~~across the globe~~ including
Shanghai and ~~Los Angeles~~ ~~LA as of this analysis but have recently been generalized to the entire globe (Demuzere et al., 2022).~~

To relate ER_{CO} to heavy industry, the percentage of heavy industry is first interpolated at 1 km grid spacing from WUDAPT
LZC maps (~~%~~, **Fig. 4c, f**). ~~Those industry coverage are~~ ~~The industrial coverage map is~~ then convolved with the X-STILT
column footprint (**Supplementary Fig. ??**) to quantify the industrial influence on each TROPOMI polygon $P_{ind}(x, y)$, which
400 is defined as the column footprint-normalized industry fraction (**Supplementary Fig. ??**). For example, soundings in the city
center farther away from the heavy industry ~~in LA~~ are related to smaller influences. Lastly, we sum $P_{ind}(x, y)$ across the
space to arrive at $\langle P_{ind} \rangle$, serving as a metric of how much the ~~FF-enhancement observation~~ at a given sounding is affected by
heavy industry. ~~Soundings Specifically, soundings~~ with $\langle P_{ind} \rangle$ larger than the 75th or 90th percentiles are marked as locations
“impacted” or “strongly impacted” by heavy industry within the city. Sensitivity and significance analyses are conducted and
405 presented in **Sect. 3.2.2** to test if: 1) the results are subject to the percentile threshold ~~for defining industry-dominant when~~
~~defining industry-dominated~~ soundings, and; 2) ERs over ~~industry-dominant industry-dominated~~ soundings are statistically
significantly different from ~~ERs for~~ the remaining soundings.

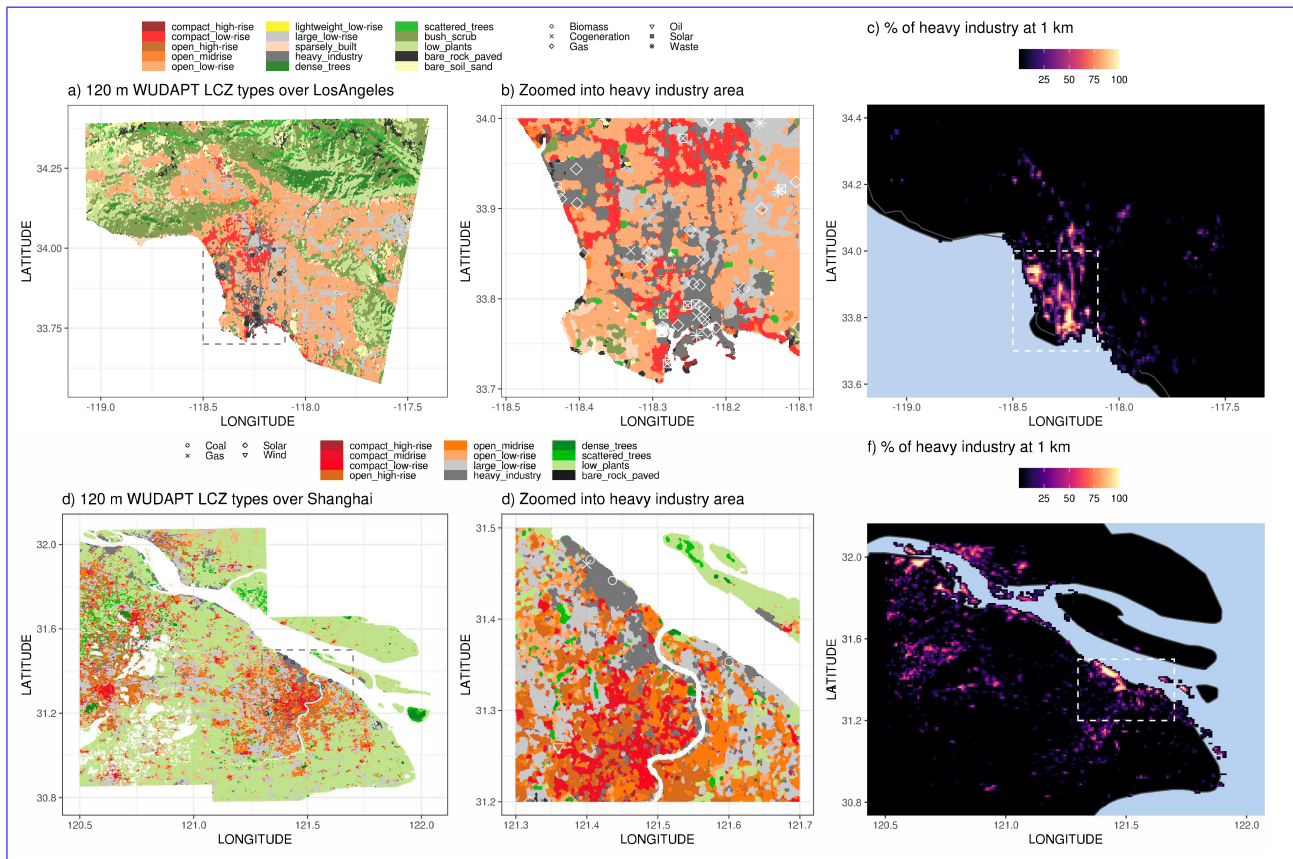


Figure 4. Maps of 120 m Local Climate Zone (LCZ) from WUDAPT (a and d) with magnified images (b and e) and an interpolated areal coverage of heavy industry [%] at 1 km around Shanghai and Los Angeles (c, f). LCZ classifications centered on Wuxi and Shanghai are combined. Power stations based on the Global Power Plant Dataset (WRI, 2018) are drawn as white symbols. The dashed light gray or white rectangles in the maps indicate the magnified region.

3 Results

ER_{CO} values and uncertainties are reported at multiple spatial scales, originating from the spatially-explicit sounding-level from the spatially-resolved sounding level (Eq. 3) to the overall overpass- and city-level. Again, only ERs at soundings within the urban plume are selected. Overpasses with too low valid soundings few valid soundings in a plume area are also removed from the results. Before presenting ERs at different spatial scales, we assess the few factors that may influence the derived ER_{CO}.

3.1 Interference factors that modify ER_{CO}

We examine the impacts on ER_{CO} from the following interference factors: 1) differences in AKs between OCO-2/3 XCO₂ and TROPOMI XCO; 2) shifts in wind fields induced by asynchronous between two overpass times; and, 3) urban-background contrast in biogenic and pyrogenic contributions; and, 4) temporal variation in emission themselves. In summary, we found

that difference in AKs and wind directions between sensors can significantly affect the spatially-resolved ER_{CO} . **After removing the overpasses substantially interfered by wind shift from consideration, biogenic and** For the final 24 overpasses we selected, temporal variations in the emission pattern and urban-background gradients in biogenic/pyrogenic contributions play a **minor role in the overall minor roles in** overpass- or city-level ERs.

The sensor-specific Recall that sounding-specific AKs and wind speed were incorporated into the calculation of species-specific column footprint in speeds were being considered in the sounding-specific column footprint using X-STILT as introduced in (Sect. 2.2. By looking at -) and the $\gamma_{foot} = \frac{\langle XF_{CO_2} \rangle}{\langle XF_{CO} \rangle}$ (Supplementary Fig. ??d), one can tell the impact on suggested their combined impacts on spatially-resolved ER_{CO} due to mismatches in AKs and wind fields between sensors (Supplementary Fig. ??c). For instance, mean γ_{foot} spans from 1.20 to 1.54 over Los Angeles 1.57 over LA and from 1.02 to 1.38 over Shanghai across different overpasses (printed in Fig. 7a, c). γ_{foot} is generally larger than 1 because the TROPOMI XCO-AKs near the surface are less than 1 and smaller than of TROPOMI XCO are smaller than surface AKs for OCO-2/3. Simply using enhancement ratios without accounting for mismatches in AK and wind speed AKs and wind speeds between sensors will likely lead to an underestimation of the emission ratios (Eq. 3). On average, overpass-level ER_{CO} can be about $\sim 20\%$ higher than the enhancement ratio for the examined cases enhancement ratios across our 24 overpasses.

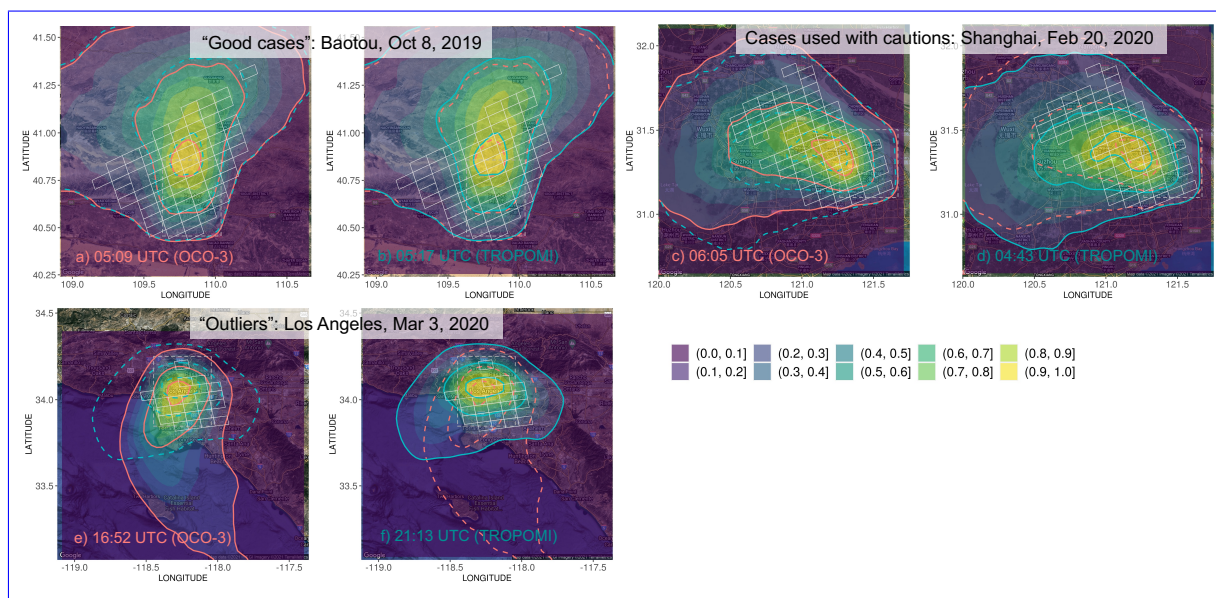


Figure 5. Examples of modeled urban plumes during OCO-3 (red curve) and TROPOMI (blue curve) overpass times in UTC. The likelihood of these meteorology-only urban plumes (no emission involved) is quantified by the normalized KDE binned by 10 intervals of the modeled air parcel distribution (yellow-green-purple contours). Three types of overpasses are shown as follows: 1) “good cases” with almost identical urban plumes at two times, e.g., Baotou on Oct 8, 2019 with Δt of 8 mins (a, b); 2) cases to be used with caution where the urban plume shifts from one time to another and requires a simple plume rotation, e.g., Shanghai on Feb 20, 2020 with Δt of 1.5 hours (c, d); 3) outliers where two urban plumes change significantly, e.g., for Los Angeles on March 3rd, 2020 with Δt of over 4 hours (e, f). The underlying hybrid maps were created using the ggmap library in R with the hybrid view of Google Maps over LA (copyright: Map data ©2021 Imagery ©2021 TerraMetrics).

The second factor is the ~~changes-change~~ in wind directions between two overpass times, which is evaluated using the same ~~approach for identifying the urban plumes algorithm as the urban plume detection~~ in Sect. 2.2.2. Again, ~~these~~ colored contours and curves in Fig. 5 ~~do not indicate~~ indicate neither the intensity of ~~concentration-concentrations~~ nor flux fields (as no ~~emission-is~~ emissions are used), but rather the likelihood of urban plumes ~~solely~~-determined by atmospheric dispersion with random wind uncertainties. Matching between OCO-3 soundings and TROPOMI polygons as described earlier would be fine for concurrent observations (~~e.g., “good cases” with almost identical plumes at two times in Fig. 5a, b~~); but becomes problematic if Δt ~~is large~~ (~~e.g., becomes large~~ (“outliers” with significant changes in ~~urban plumes in~~ plumes in Fig. 5e, f). ~~Since no simple wind or plume rotation would improve the ER estimates, cases with > 3 hours are removed from this analysis.~~

440 The cases between ~~the~~ “good cases” and ~~the~~ “outliers” are ~~cases~~ to be used with caution (Fig. 5c, d). By comparing the overlap of plumes at the two times, we ~~then shifted the~~ shifted OCO-3 soundings to better align with ~~the~~ TROPOMI polygons. For example, on Feb 20, 2020, because the modeled plume at the OCO-3 overpass time (06:06 UTC) appears northward compared to the plume at the TROPOMI overpass time (04:44 UTC), ~~soundings at the OCO-3 overpass time soundings~~ were shifted southward by 0 to 2 grids depending on their longitudinal coordinates (Supplementary Fig. ??). In other words, by

445 shifting ~~the observed~~ FF XCO₂ enhancements, we better align the urban plume at OCO-3 time with the plume at TROPOMI time. Every OCO-TROPOMI coincidence has been manually examined and assigned to one of the three categories, which are further summarized in Sect. 4.1. “Outliers” are removed from this analysis, since no simple wind or plume rotation would improve their ER_{CO} estimates.

Examples of modeled urban plumes during OCO-3 (red curve) and TROPOMI (blue curve) overpass times (in UTC labelled

450 ~~on the bottom of each panel~~). The likelihood of these meteorology-only urban plumes (no emission involved) is quantified by the normalized KDE (10 intervals in the color legend) of modeled air parcel distribution (yellow-green-purple contours). Three types of overpasses are shown as follows: 1) “good cases” with almost identical urban plumes at two times, e.g., Baotou on Oct 8, 2019 with of 8 mins (a, b); 2) cases to be used with caution where the urban plume shifts from one time to another and requires a simple plume rotation, e.g., Shanghai on Feb 20, 2020 with of 1.5 hours (c, d); 3) outliers where the urban plumes

455 ~~change significantly, e.g., for Los Angeles on March 3rd, 2020 with of over 4 hours (e, f). Outliers with of over 3 hours are removed from the final results.~~

The last factor is the urban-background contrast due to non-FF sources/sinks. Although LA is surrounded by occasional intense wildfire activities, column anomalies due to biomass burning suggested by the coupling of GFAS and X-STILT are minimal for the dates we examined. However, since fire-related ~~Besides changes in wind directions, CO and CO₂ emissions~~

460 themselves can vary across daytime hours, likely driven by the road transportation and residential sectors. As a result, variations in the derived ER_{CO} are mostly higher than FF-related (across multiple overpasses may reflect not only the variation in combustion efficiencies but also the mismatch in the emission timing. LA may be one of the cities with more distinct daytime changes in emissions compared to industry-centered cities. Fortunately, based on a supplementary sensitivity analysis using measurements from the Total Carbon Column Observing Network in Pasadena (TCCON, Wennberg et al., 2017), by limiting

465 satellite overpasses to those with a smaller time difference, ER_{CO} appear to be less variable (Supplementary Fig. 1??), properly accounting for pyrogenic contributions and gradients in. Future geostationary satellite monitoring NO_x (e.g., TEMPO, Chance et al.

provide better guidance towards the hourly pattern in urban emissions, especially from the traffic sector with more daytime fluctuations, which have been discovered using surface monitoring networks (e.g., over Chicago; de Foy, 2018).

The last factor is ~~the enhancement is important for cities in mountainous and forested areas during the fire season (e.g., Mexico City and LA).~~ The sounding-specific urban-background contrast in contributions from non-FF sources and sinks. The modeled biogenic XCO₂ anomalies anomaly using SMUrF and X-STILT ranges from -0.7 to 0.3 ppm per OCO-3 sounding, depending on the ~~season and the hour of a day (i.e., solar zenith angle),~~ season and wind direction (**Supplementary Fig. ??**) ~~and are further aggregated to the TROPOMI scale.~~ As explained ~~above, strong in Sect. 2.2.2,~~ urban-background gradients in these biogenic anomalies (i.e., δX_{bio}) ~~may alter the FF enhancement and, so such gradients~~ were used to correct the constant localized background X_{bg} (**Eq. 1**). Take the two overpasses with the largest urban-background contrast as examples: as biospheric uptake is normally weaker in urban areas than surrounding rural areas (often as background regions), the urban-rural gradient for locations in the plume region becomes more positive (**Supplementary Fig. ??b**). Nonetheless, even for the one summertime SAM over Zibo on June 21, 2020, sounding-level δX_{bio} ranges from 0 to 0.4 ppm, which remains small compared to sounding-level FFCO₂ enhancements of 2 to 7 ppm (**Supplementary Fig. ??a, b**). For most other overpasses, ~~urban-background~~ δX_{bio} ~~remains aggregated to TROPOMI sampling stay low with an absolute value < 0.2 ppm-0.3 ppm (as printed in each panel of Figs. 6 & 7).~~ Even with a bias in the resultant δX_{bio} (~~resulting from uncertainties in prior NEE~~) resulting from incorrect prior NEE, the effect on derived FF enhancements and ER_{CO} would be small.

Although LA is surrounded by occasional intense wildfire activities, column anomalies due to biomass burning suggested by the coupling of GFAS and X-STILT are minimal for the dates we examined. Yet, since wildfire-related ER_{CO} are usually higher than FF-related ER_{CO} (Fig. 1), the proper account of pyrogenic contributions and gradients between urban and surrounding rural areas is important for cities in mountainous and forested areas during fire seasons. For instance, Crouse et al. (2009) leveraged aircraft measurements of HCN and C₂H₂ over Mexico City as indicators to disentangle CO signals due to biomass burning and urban emissions, respectively.

3.2 Intra-city ER_{CO} variations and ~~signal~~ signals from heavy industry

~~The measured concentration~~ Observed enhancements are the net consequence of associated sources/sinks from source regions. That is, high atmospheric content of CO₂ or CO at the sounding location does not necessarily indicate a high emission rate at this location (Kiel et al., 2021). Our derived emissions and ERs, although reported for each sounding, indicate the overall emission and combustion efficiency over its source region.

In the following subsections, we present ERs ~~from sounding-level to the overpass and city-level~~ for each sounding and the aggregate for each overpass and city. Since aggregating ~~spatially-explicit~~ sounding-level ERs to a single value per overpass or city is sensitive to the adopted method/~~statistics and the overpass-specific atmospheric movement~~ statistic, we bootstrapped ~~ECO and E based on sounding-level emissions and uncertainties 5,000 times and applied linear regression fits (e.g., E_{CO} and E_{CO2} based on their sounding-specific values and uncertainties to generate a linear regression fit per bootstrap loop~~ (light grey lines in **Fig. 6**). Specifically, 51,000 random sets of ~~ECO and E_{CO} and E_{CO2}~~ were generated following assumed normal distributions, where sounding-level ~~emissions denote the mean statistic with observed and background uncertainties as the standard~~

deviation (SD) statistic emission estimates provide mean statistics with observational uncertainties as standard deviations. We used the standardized major axis (SMA) solution for linear regression to minimize the deviation of the data point deviations of data points from the regression line for both axes. Eventually, we obtained 51,000 bootstrapped slopes and only selected slopes with positive values, of which mean values and SDs which yield the overpass-level ER_{CO} values and uncertainties (and uncertainty (e.g., colored dashed lines and text in Fig. 6). Sounding-level Besides, sounding-level ER_{CO} values from all overpasses are also presented in histograms, which and generally follow a log-normal distribution (Figs Fig. 7b, 7dd).

City	Total power capacity (MW) and by fuel types	Key industry OR annual crude steel capacity (kt yr ⁻¹)
Los Angeles	5,808 MW (95.6% fueled by gas; 0% by coal)	refinery, shipping
Shanghai	16,031 MW (75.2% fueled by coal; 24.4% by gas)	iron & steel (25,099 kt yr ⁻¹)
Baotou	6,470 MW (100% fueled by coal)	iron & steel (12,619 kt yr ⁻¹)
Zibo (w/ Zouping)	9,720 MW (100% fueled by coal)	electrolytic aluminum; iron & steel (2,532 kt yr ⁻¹)

Table 1. A summary of total power generation capacity (Global Power Plant Dataset by World Resources Institute, 2018) and information on heavy industry including annual crude iron capacity (GID, Wang et al., 2019). Power plants are selected from a 0.5° × 0.5° region around each city with percentage generated by the main fuel types.

3.2.1 Baotou and Zibo

Combustion efficiencies are generally poor for these two industry-oriented industry- and energy- oriented cities. The overpass-specific ERs span from 8.19.3±1.3 to 26.71.2 to 24.6±3.8 mmol mol⁻¹ with an integrated city-level estimate of 18.417.3±0.6 0.5 mmol mol⁻¹ for Baotou (Fig. 6a). According to GID, the Baotou iron and steel group is located in within the city and contributes to an annual capacity of crude iron of 12,618.91 kt 619 kt yr⁻¹ with estimated CO₂ emissions of 20,462 kt per year. The relative low yr⁻¹ (Table 1). The slightly lower ER_{CO} and FF enhancements in Feb 2021 coincides with the timing of the Spring Festival in 2021. SDs of the 2021 (~Feb 12). SDs of bootstrapped slopes are higher for overpasses with fewer high-quality satellite soundings, e.g., 3.8 mmol mol⁻¹ for overpasses with 7 available urban TROPOMI polygons over Baotou seven available TROPOMI polygons in the urban plume on May 31, 2020, which helps minimize 2020. Utilizing the bootstrap method helps account for the impact of low-sounding numbers on the overall city-level ER estimates estimate.

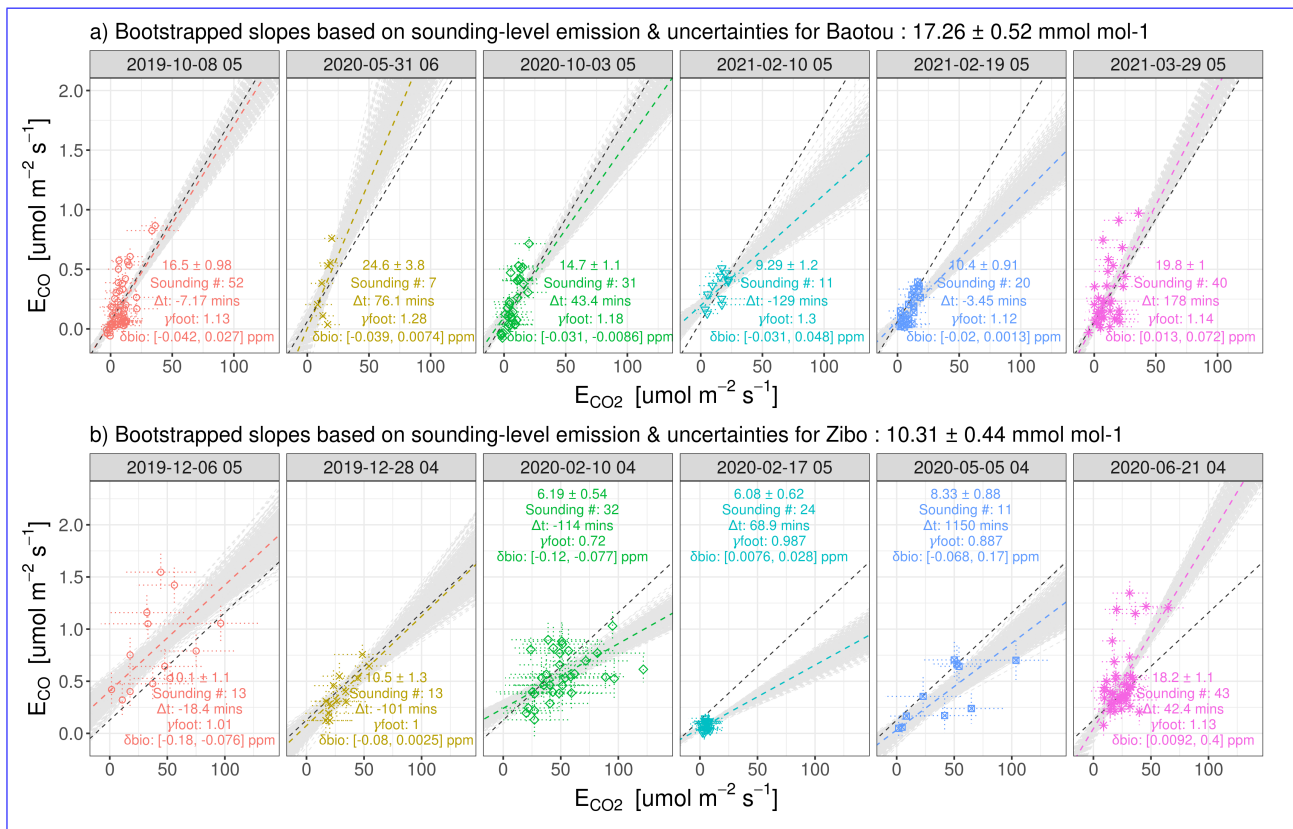


Figure 6. Scatter plot-plots of CO and CO₂ fluxes [$\mu\text{mol m}^{-2} \text{s}^{-1}$] and their uncertainties (error bars in dotted lines) for Baotou (a) and Zibo (b). Data for all overpasses are from OCO-3 SAMs, except for the first two overpasses for Zibo (OCO-3 Nadir). Linear regressions using the standardized major axis (SMA) method are applied for the data from each overpass (dashed colored lines) and all overpasses (dashed black line). Only bootstrapped regression lines with positive slopes were chosen from the Monte Carlo experiment (dashed gray lines; $\sim 98.4\%$ and 93.3% of the total 6,000 bootstrapped lines for Baotou and Zibo, respectively). TROPOMI overpass time in UTC, total TROPOMI sounding numbers, discrepancies in overpass time-between-OCO-and-TROPOMI-times (Δt , mins), impacts from AK and atmospheric-transport-wind conditions between sensors (γ_{foot}), and the range of urban-rural biogenic gradient ($\gamma_{\text{bio}}\delta X_{\text{bio}}$, ppm) are labelled on-in each panel. XCO₂ on Dec 6 and Dec 28, 2019 over Zibo are the Nadir OCO-3 observations. Feb to May in 2020 is the time frame for the initial phase of the COVID-19 lockdown in China.

520 Interestingly, the ER for Zibo first dropped from 11.0 Zibo with the nearby county-level city Zouping accounts for over 1/8 of the total coal consumption of Shandong province in 2017. The coal-fired power plants in the area contribute to a total power generation capacity of 9,720 MW (Table 1), which are likely to support local metal industries especially the production of electrolytic aluminum (world's top producers). The maximum XCO₂ enhancement per OCO-3 sounding can even reach up to 10 ppm for a few overpasses (not shown). Interestingly, ER_{CO} for Zibo first declined from 10.1 ± 1.3 1.1 mmol mol⁻¹ to 6.36 1 ± 0.5 0.6 mmol mol⁻¹ during Feb 2020 and then gradually rose back to 20.4 gradually increased back to 18.2 ± 1.3 1.1 mmol mol⁻¹ by June 2020 (Fig. 6b). In addition to low in Feb and May 2020, their FF enhancements remain low. Such temporal variations in both-ER_{CO} and enhancements agree nicely with the timing of the initial phase of COVID-19 lockdown in China

525 (e.g., Laughner et al., 2021). (i.e., Feb to May in 2020) (e.g., Laughner et al., 2021). We suspect changes in ER_{CO} could be driven by the partial shut-down and re-opening of the multiple coal-fired power plants and metal industries in the area.

3.2.2 Los Angeles and Shanghai

Although OCO-3 has sampled the Los Angeles basin ~~several dozens of~~ times to date, ~~unfortunately, a few of them many~~ overpasses did not pass the quality check (i.e., QF) and were removed from the final result due to their ~~dramatic change in~~ wind direction noticeable shifts in urban plumes between two overpass times (e.g., ~~>3 hours time difference on~~ March 3, April 15, and May 5, 2020 for LA; ~~see discussion; discussed~~ in Sect. 4.1). The overpass-level ER ranges from ~~7.27.4~~ ± 0.8 to ~~12.411.7~~ ± 1.3 –~~1.5~~ mmol-CO/mol-CO₂ with a city-level value of either ~~9.79.6~~ ± 0.5 mmol mol⁻¹ informed by using the regression approach (Fig. 7a) or ~~9.99.7~~ mmol mol⁻¹ by using the histogram approach (Fig. 7b). Our space-based ER_{CO} values for estimates over LA fall within the reported range of 7.1 to 12.4 mmol mol⁻¹ ~~inferred from several from~~ prior studies (Wennberg et al., 2012; Brioude et al., 2013; Hedelius et al., 2016; Silva and Arellano, 2017); ~~despite the time difference~~. Small discrepancies in ER_{CO} between studies may be attributed to discrepancies in the time of interest, sampling strategies, and techniques for ~~calculating-ER_{CO} calculations~~ (e.g., ~~exact-background locations~~); ~~background definition~~.

In contrast to LA, where urban plumes are usually well-constrained with the basin, ~~the~~ wind speeds and directions ~~change dramatically among~~ vary across different overpasses over Shanghai —i.e., southeasterly wind on Feb 4 and Feb 20, 2020; ~~;~~ southwesterly wind on Feb 24, 2020 and Feb 19, 2021; ~~;~~ and northerly wind on April 23 and Dec 30, 2020. Such changes in the wind regimes between overpasses over Shanghai suggest that ~~observations per overpass reflect fluxes soundings from an individual overpass may reflect emission patterns~~ over different source regions, which emphasizes the importance of integrating atmospheric transport in interpreting temporal variations in observation-based ERs. ~~In other words, one cannot simply use all the soundings over a city to calculate ERs, but need to select those soundings that are actually affected by emissions from that city.~~ The overpass-specific ER ranges from ~~4.74.2~~ ± 1.2 to ~~20.117.1~~ ± 7.3 –~~6.2~~ mmol mol⁻¹ with a city-level average of ~~10.510.2~~ ± 0.4 mmol mol⁻¹ based on the linear regression approach (Fig. 7c) or ~~12.9~~ mmol mol⁻¹ using the histogram approach (Fig. 7d).

a, c) Same as Fig. 6 but for LA and Shanghai. Only bootstrapped regression lines with positive slopes are presented as light grey lines. b, d) Histogram of for all soundings (black bars); soundings impacted or strongly impacted by heavy industry are defined using larger than their 75th or 90th percentiles (blue or red bars) with corresponding median ERs (vertical dashed lines). The industrial impact is quantified using column footprints from X-STILT (to inform atmospheric transport) together with localized information from the urban land cover data WUDAPT.

Histograms for the ~~Now we focused on the distribution of~~ sounding-level ERs within the LA basin and the greater Shanghai area are shown in Fig. 7b,d, respectively for these two megacities (Fig. 7b, d) to see if ERs associated with a part of the city (i.e., heavy industry region) can be revealed. As described earlier, to address the overpass-specific meteorology, we coupled the LZC-based industrial coverage with X-STILT column footprints to locate the soundings affected or strongly affected by heavy industry in a city. ~~For example, on Feb 20, 2020 the few soundings with of >75th percentiles (outlined in black in with the account of overpass-specific meteorology, we coupled the LZC-based industrial coverage~~ (Supplementary Fig. ??4c, f) are

identified as soundings affected by industry with X-STILT column footprints and quantified the industrial influence, $\langle P_{ind} \rangle$, at
560 each sounding location.

Heavy industrial/Industrial regions within the LA basin are concentrated to the south (e.g., near the Port of LA) and to the west of downtown near Los Angeles Airport and the Chevron Refinery in El Segundo (Fig. 4e). The distribution of ERs for industry-dominant soundings tend industry-dominated soundings tends to shift slightly towards the lower end (blue or red bars in Fig. 7b) compared to the distribution for all soundings (black-gray bars in Fig. 7b). Specifically, For example, ERs > 20 – 15 ppb
565 ppm^{-1} are less frequently found for industry-dominant industry-dominated soundings (red bars in Fig. 7b). It is worth noting that the The industry-oriented soundings generally have slightly lower CO but higher CO₂ enhancements (Supplementary Fig. ??a, 2b, c), compared to all other soundings within the valley basin, resulting in slightly lower ER_{CO} (Supplementary Fig. ??e). No iron and steel facilities or coal-fired power plants are found over the heavy industry area in LA according to
570 GID and GEM. We hypothesize that the slight shift of ER_{CO} towards the lower end may be explained by the heavy-duty diesel engines and natural gas power plants occupying the Port of LA versus the predominately gasoline vehicles across the city, because ER_{CO} for heavy-duty diesel vehicles and non-coal-fired power plants are generally lower than that for light-duty gasoline vehicles. For example, by splitting observations for daytime versus nighttime, a field campaign in 2007 in Beijing suggested that the ER linked to nighttime diesel transportation is much lower than the gasoline sub-sector (Westerdahl et al., 2009, Fig. 1a). Similar to LA, higher fuel efficiency has been was found over the ship channel of Houston (ER of ~ 4 ppb
575 ppm^{-1}) compared to downtown Houston (ER of ~ 10 ppb ppm^{-1}) (Brioude et al., 2012, Fig. 1b). Unfortunately, only two good SAMs are available near Houston from late 2019 to June 2021, but future work can further validate the urban-industry contrast in ERs from space.

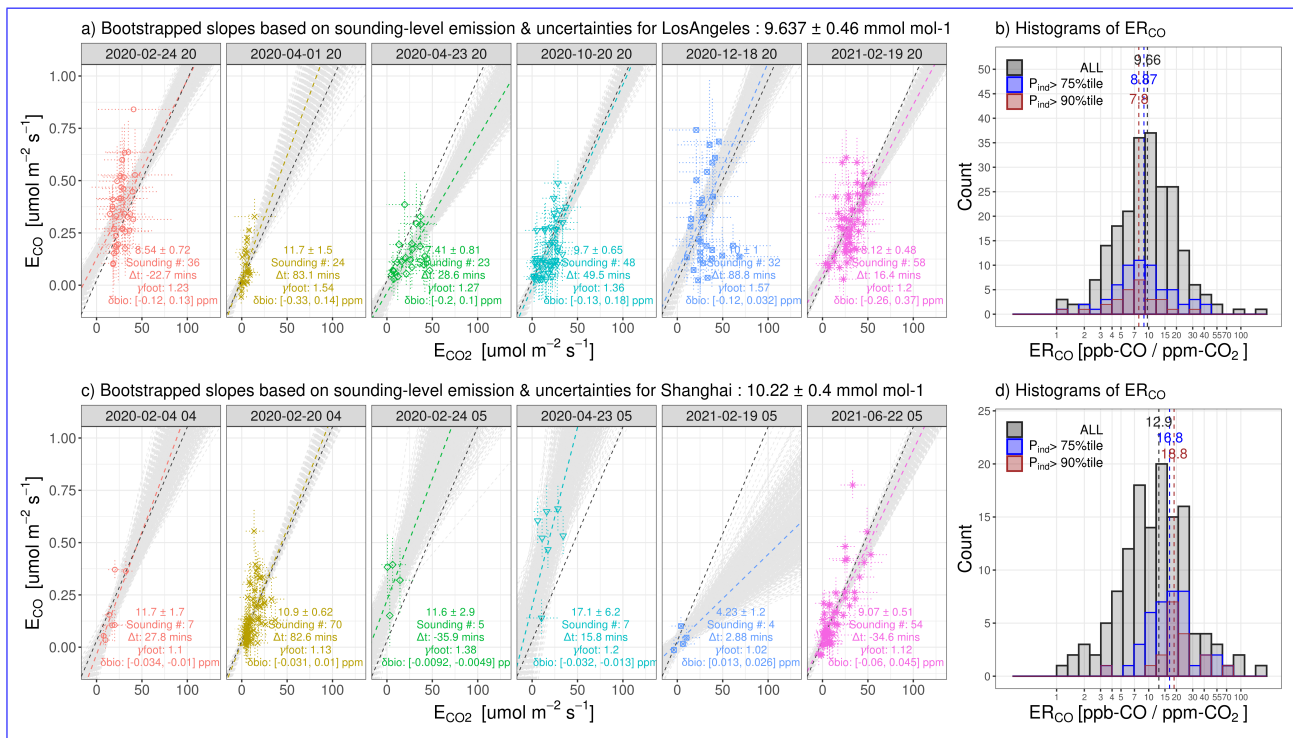


Figure 7. a, c) Same as Fig. 6 but for LA and Shanghai. Only bootstrapped regression lines with positive slopes are presented as light grey lines ($\sim 94.3\%$ and 88.4% of the 1000 bootstrapped lines per overpass for LA and Shanghai, respectively). b, d) Histogram of ER_{CO} for all soundings (black bars); soundings impacted or strongly impacted by heavy industry are defined using $\langle P_{ind} \rangle$ larger than their 75th or 90th percentiles (blue or red bars) with corresponding median ERs (vertical dashed lines). The industrial impact is quantified using column footprints from X-STILT (to inform atmospheric transport) together with localized information from the urban land cover data WUDAPT.

For Shanghai, the heavy industry is concentrated to the north of the city center (Fig. 4a). Interestingly, in contrast to LA, ERs strongly concentrated with affected by heavy industry are skewed towards the higher end with medians of 16.8 or 18.4–18.8 ppb ppm⁻¹ (blue or red bars in Fig. 7d), compared against the city-level median of 12.7–12.9 ppb ppm⁻¹ (black bars in Fig. 7d). FFCO and FFCO and CO₂ enhancements and ER_{CO} are all higher for industry-oriented soundings than those for all soundings combined. Such spatial divergence in enhancements and ERs between heavy industry and the entire city may be attributed to substantial CO emissions from iron and steel production. Schneising et al. (2019) also found that many hotspots with high TROPOMI CO enhancements in China and India are tied to iron and steel industries. During such production processes, iron ores are reduced to crude iron and steel where CO is involved. According to the plant level estimate in 2019 from GID, Baoshan Iron & Steel Co., Ltd. located to the north of downtown Shanghai has an annual crude steel capacity of 25,099.4–099 kt yr⁻¹ (Table 1) and a total CO₂ emission of 32,148.0–148 kt yr⁻¹ for all coke, sinter, iron, and crude steel combined.

Finally, to validate the To validate the robustness in such ER shifts related to heavy industry within an urban area, we tested different percentile thresholds other than the default 75th and 95th for determining industry-dominant used to determine industry-dominated soundings (Sect. 2.3). The above statements on industry-impacted ER_{CO} hold if using alternative thresh-

olds including the 50th, 60th, 80th percentiles. Additional Welch two-sample t-test confirms that ERs from ~~industry-dominant~~ industry-dominated soundings significantly differ from the remaining soundings (~~i.e., less affected by industry~~) heavy industry. When the adopted percentile threshold increases from 50th to 95th, divergence in ERs between industrial vs. non-industrial soundings becomes more apparent and the p-value for statistical significance in such difference becomes smaller (with p-values < 0.05) ~~)-Also for all thresholds~~. In addition, the average number of OCO-3 soundings in a TROPOMI polygon is roughly the same for industry-affected soundings versus the rest (e.g., 11.8 vs. 10.3 for LA and 7.3 vs. 8.7 for Shanghai).

We ~~note that it~~ acknowledged that although many iron/steel plants may aim at combusting as much CO as possible before releasing CO into the atmosphere, the indispensable role CO played in the iron/steel industry makes it unique when assessing its ER_{CO} and combustion efficiency among various industrial processes. Furthermore, it is difficult to separate ~~individual sectoral signals purely from observations~~ (combustion signals of individual sectors from observations without prior assumptions on ~~sectoral contributions~~) sector-specific contributions, since atmospheric concentration at a given location is comprised of various underlying burning combustion processes spread over the source region. Even using additional co-emitted species, it would be risky to assume that a co-emitted species (e.g., CO or NO_x) solely comes from one individual emission sector.

4 Discussion

This study is one of the first to analyze intra-city variations of emission ratios between CO and CO₂ using two asynchronous satellite sensors. We describe 1) complications induced by discrepancies between satellite sensors and retrievals and 2) demonstrate methods to mitigate these complications by accounting for ~~species-specific averaging kernels~~ sounding-specific averaging kernels, atmospheric transport, and urban-background contrast in the contribution from non-FF sources/sinks using an atmospheric transport model.

4.1 Influence from non-FF components and atmospheric transport

~~The pyrogenic~~ Pyrogenic anomalies are minimal for the overpasses we examined, but should be considered for certain cities (e.g. during dry seasons over Mexico City, Crouse et al., 2009) considering the high ER_{CO} from forest wildfires of 35 to 80 ppb ppm⁻¹ (**Fig. 1a**). Most overpasses we analyzed fall within the dormant seasons. For the three overpasses during the growing season, modeled biogenic anomalies using the SMUrF model for a given OCO-2/3 sounding may reach up to 0.5 ppm (**Supplementary Fig. ??**). Even though modeled NEE and resultant biogenic contributions/gradient can be uncertain, we stress again it is the urban-background biogenic contrast (δX_{bio} in **Eq. 1**) that ~~should be considered for when is important~~ for estimating FFCO₂ enhancements given our setup for a local background value. Satellite missions such as TROPOMI and the upcoming Geostationary Carbon Cycle Observatory (GeoCarb) will ~~also provide the~~ provide Solar-Induced Fluorescence (SIF), which may help improve spatially-explicit SIF-based GPP and NEE estimates (Turner et al., 2020; Wu et al., 2021), specifically by reducing the dependence on other remote sensing products and the assumption of model parameters for each plant ~~function~~ functional type.

The biggest challenge ~~interfering the robust affecting the robust estimate of~~ spatially-resolved ER estimates is the wind directional shift induced by the lack of concurrence between sensors. ER_{CO} is the shift in wind directions between two overpass times. Substantial changes in the wind direction and resultant wind directions and urban plumes (e.g., the “outlier” case in “outliers” in Fig. 5e, f) were mostly found for overpasses when absolute time differences with an absolute time difference $|\Delta t|$ were of > 2 hours (implied by the bars with white strips and asterisk on top attached with an asterisk in Fig. 8). However, if TROPOMI pixel sizes are relatively large (i.e., non-nadir observations) or the wind is steadier, this $|\Delta t|$ constraint can be relaxed. ~~may be relaxed, as long as emissions for a specific city is less driven by sectors with noticeable diurnal cycle (e.g., road transportation).~~ For instance, TROPOMI polygon sizes for Baotou on May 31, 2020, TROPOMI polygon sizes for the industry-dominated city Baotou are sufficiently large compared to the shift in urban plumes despite its $|\Delta t|$ of 3 hours (Fig. 8). ~~Because of this, we decided to exclude overpasses with $|\Delta t| > 3$ hours.~~ In addition, we manually re-positioned the OCO-3 soundings to TROPOMI polygons for a few cases (bars with non-zero numbers on top in Fig. 8) using a simple wind/plume shift demonstrated in Sect. 3.1. Fortunately, future geostationary satellite satellites will be capable of mapping XCO and XCO₂ spontaneously simultaneously at a higher temporal frequency, which will eliminate this issue.

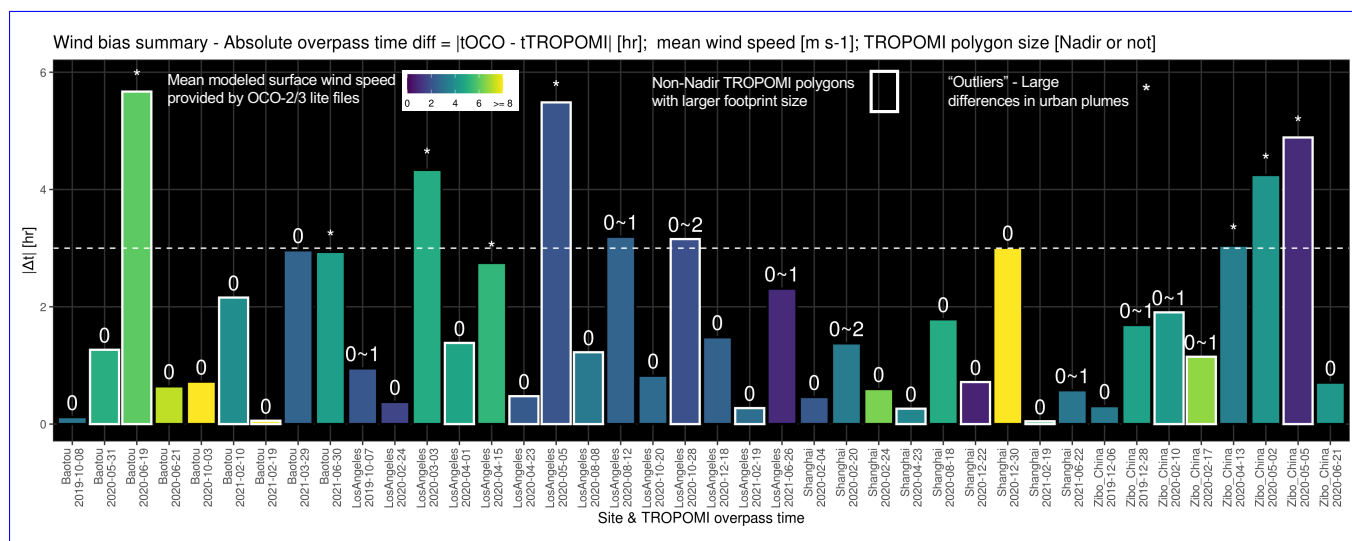


Figure 8. A summary figure of the investigation on the wind directional shift between OCO-2/3 versus TROPOMI overpass times. The y-axis denotes the absolute time difference ($|\Delta t|$ in hours) for multiple overpasses per overpass. The colors of the bars represent the instantaneous modeled surface wind speed [m s⁻¹] provided by from OCO-2/3 Lite files. Bars labelled with an asterisk indicate that urban plumes between two overpass times differ significantly so much that they cannot be brought into agreement with a simple plume rotation fails to fix. The number on each bar (e.g., 0~1) denotes the number of TROPOMI polygons needed to be shifted to align the urban plumes at two times. “Good Cases” For example, 0~1 means that TROPOMI polygons over certain locations are shifted by one grid. Bars labelled with zero on top do not require a manual plume shift (bars with zero labelling). Bars outlined in white indicate that the sampled TROPOMI soundings on that date are non-nadir with larger pixel size.

635 4.2 ERs ~~per for individual sounding, per-overpass, city, and per-heavy industry region within a city~~

Contrary to previous work relying on inventory-based sector-based ERs, we attribute the intra-urban gradient to heavy industry using ~~a an~~ urban land cover classification dataset. Such high-resolution localized maps help ~~guide the identification of identify~~ ~~the~~ observations strongly influenced by heavy industry. Based on a limited sample size, the heavy industry within the greater Shanghai area is tied to an ER_{CO} higher than the city average reflecting a ~~poor-relatively poorer~~ combustion efficiency (**Fig. 7d**). ~~Industry-oriented-Industry- and energy- centered~~ cities like Baotou and Zibo are less efficient in their ~~burning-combustion~~ activities. In particular, ~~industry-dominant-industry-dominated~~ ERs over Shanghai (~~20.9-18.8~~ mmol mol^{-1} as indicated by the ~~red bars-dashed red line~~ in **Fig. 7d**) align better with the overall city-scale ER over Baotou ~~or Zibo (24.1 or 20 of 17.3~~ mmol mol^{-1} , (**Fig. 6**). The previously reported urban-integrated ER_{CO} values are mostly constrained within the range of 5 to 20 ppb ppm^{-1} with a few exceptions over 30 ppb ppm^{-1} in east Asia before 2010 (**Fig. 1**). ~~The order of magnitude of our~~ ~~Our~~ city-level estimates from space agree well with ~~that the range~~ of previously reported ~~ERs values~~.

Reporting one city-scale ER_{CO} from spatially-explicit ERs can be ~~subjective-subject~~ to 1) the adopted ~~statistics-statistic~~, 2) ~~the overpasses and their associated wind regimes-overpass dates and overpass-specific wind conditions~~, and 3) estimated uncertainties in ER_{CO} . For example, overall ER ~~based on-derived from~~ all soundings within the urban plume differs from ~~ERs ER derived~~ from a selection of soundings. ~~ERs between overpasses over Shanghai can vary due to changes in the wind fields and source-receptor geometry~~. Even though we ~~begun with all available-started with all quantified~~ OCO-2/3 observations in a SAM, only ~~soundings-those~~ located within the urban plumes (black curve in **Fig. 3**) ~~are selected for ER estimates can be used to estimate ERs~~, which is an unbiased way to ~~assess-different-compare ERs from~~ overpasses with different meteorological conditions. The mean or median value of sounding-level ER_{CO} (e.g., 13.4 or 9.6 ppb ppm^{-1} for LA in **Supplementary Fig. ??**) differs ~~slightly~~ from the city-average ~~when~~ using the regression slope method ~~that take observational uncertainties when~~ ~~observational uncertainties were taken~~ into account (e.g., ~~10.59-9.6~~ ppb ppm^{-1} for LA in **Fig. 7a**). Apart from these bulk quantities, ~~intra-city distributions of ERs are negatively-skewed-the distribution of~~ ER_{CO} in the linear space ~~are negatively-skewed~~ and roughly follow the ~~normal-distribution-in-natural-log-space-log-normal distribution~~ (**Supplementary Fig. ??**), where a few observations with higher ER_{CO} are influenced by point sources with poorer combustion efficiency. More observations with finer satellite pixels across the city would improve the robustness in both the spatial distribution and ~~the~~ bulk estimates of ERs.

660 4.3 Limitation~~and implications~~

The main limitation of this work is the relatively low sample size ~~largely constrained by the requirement for small differences in overpass times~~. When more satellite data ~~or upcoming data from geostationary satellites~~ become accessible, intra-city ERs can be used to more robustly ~~re-assess the temporal variations-assess the temporal variation~~ in sector-oriented combustion efficiency, including across ~~different seasons and seasons or times (e.g.,~~ business-as-usual scenarios versus pandemic-disturbed time frames). Beyond the sheer number of soundings, uncertainty arises ~~due to the aggregation of when aggregating~~ CO_2 enhancements from the finer resolution OCO-3 grid to ~~coarser-TROPOMI spatial scale~~ ~~the TROPOMI sampling~~. The centered lat/lon coordinates of OCO-2/3 soundings are ~~used to decide which~~ ~~chosen to decide the~~ corresponding TROPOMI polygon~~they~~

670 ~~fall into~~, while a very few OCO soundings may ~~locate~~ be located right on the boundary of TROPOMI polygons. Nevertheless, we find no significant bias associated with the number of OCO soundings per TROPOMI polygon. ~~The variability from different OCO soundings within a given TROPOMI polygon serves as the “observational noise” in the uncertainty regarding the heavy industry~~ analysis.

~~We then discuss the impact on our results given the lack of consideration of the secondary CO source~~ Another factor that we did not explicitly account for is the secondary CO production from both anthropogenic and biogenic VOCs (AVOCs, BVOCs). Under a cascade of reactions in favorable conditions, VOCs ~~can be emitted from the upwind source location~~ are oxidized to CO at various rates, ~~relying on the amount, speciation, and reactivity of VOCs. The lifetimes of and certain VOCs species against OH radical are long enough compared to our time of interests, i.e., a few hours before overpass time to render their impact negligible in this analysis. BVOCs (e.g., isoprene) and a subset of the anthropogenic VOCs (e.g., alkenes) react quickly and often generate HCHO (e.g., Surl et al., 2018) which subsequently can be photochemically converted to CO in a few hours. For example, isoprene contributed to 21.2% of which result in possible higher CO at the downwind sounding location and a~~ divergence between enhancement ratios and emission ratios. As BVOCs are usually associated with shorter lifetimes compared to many AVOCs (e.g., Surl et al., 2018), we discuss BVOCs and AVOCs separately. BVOCs can contribute significantly to the total CO sources from June to August, but negligible amount from March to April over Alaska (Miller et al., 2008). Most of our overpasses fall within the non-growing season, the CO produced by BVOCs may likely be encapsulated in the background XCO and yield a small impact on our results. Regarding industrial areas with possible higher AVOCs than urban cores, e.g., ~~over Houston in Aug 2000 (Czader et al., 2008), whether AVOCs produce significantly more CO over industrial areas than urban cores within the time period of interest remains unclear. Owing to the lack of observations for the source at the regional scale especially during growing seasons (e.g., Miller et al., 2008; Hudman et al., 2008; Gonzalez et al., 2021). However, since BVOCs like biogenic CO₂ come mainly from rural areas outside the city, by subtracting localized CO background using CO observations outside the urban plume, the impact from BVOCs on the derivation of CO enhancements would be minimized.~~ The lifetime of most AVOCs remains long enough, except for a few species including alkenes (Surl et al., 2018). Without a good observational constraint of the VOC composition and species-specific emissions in the air mixture over different cities and parts of a city, it is group-specific emissions for different cities around the globe over the years, it would be challenging to accurately quantify the intra-city variation in secondary CO production and isolate such variation from the observed XCO variability. ~~impact on atmospheric XCO and ER_{CO} due to AVOCs emitted from urban areas or specifically from industrial~~ areas. More future efforts regarding urban VOCs may include 1) exploring what good proxies can be measured from space that well represent the bulk AVOC characteristics (e.g., formaldehyde, Zhu et al., 2014) and 2) interpreting such observations, e.g., by utilizing chemical transport models for source attribution (Gonzalez et al., 2021). Note that the noise/uncertainty in current daily TROPOMI formaldehyde observations may be too large for daily resolved analyses.

~~This work also provides some~~

700 4.4 Implications for inventory evaluation

This work provides insights towards estimating emission ratios from future satellite sensors, as ERs help pinpoint hotspots with poor combustion efficiency ~~can help~~, which to inform sub-city emission/pollution control efforts.

Satellite-based ER ~~may help evaluate sectoral estimates help evaluate sector-specific~~ emission factors and source locations adopted in bottom-up emission ~~inventory inventories~~ (e.g., Silva and Arellano, 2017). Substantial contrast in both the
705 magnitude and spatial distribution of enhancement ratios can be found between the observations and forward simulations ~~based on~~ (using X-STILT column ~~footprint footprints~~ and sectoral emissions from EDGARv5. ~~Over Shanghai, for example,~~ enhancement ratios simulated using the industry emissions from EDGAR are located far south (**Supplementary Fig. ??c**), compared to the observed enhancement ratio in **Supplementary Fig. ??a**. Additionally, the simulated enhancement ratios (**Supplementary Fig. ??b**) are generally too high (e.g.,). Take Shanghai as an example, simulated enhancement ratios using
710 prior emissions appear to be much higher ($> 50 \text{ ppb ppm}^{-1}$) ~~compared to~~, **Supplementary Fig. ??b**) than observed ratios (mostly $< 30 \text{ ppb ppm}^{-1}$). **Supplementary Fig. ??a**. Regarding the spatial distribution, simulated enhancement ratios using total FF emissions mimic simulated enhancement ratios using only industry-related emissions (**Supplementary Fig. ??b versus c**); and both simulated ratios differ substantially from observed enhancement ratios. Such model-data mismatch may result from inaccurate activity data and emission factors ~~when constructing the bottom-up flux estimates of EDGAR~~ as well
715 as ~~from uncertainties in the atmospheric transport. The simple example atmospheric transport uncertainties. This preliminary analysis~~ illustrates that satellite observations of trace gases could be used to evaluate emission factors ~~used adopted~~ in bottom up emission ~~inventory inventories~~. More sophisticated approaches such as flux ~~inversion~~ (Hedelius et al., 2018; Brioude et al., 2011, 2012; Palmer et al., 2006) may better constrain sector-specific CO and CO₂ emissions from inventories.

720 Spatial proxies including nightlight data from the Black Marble (<https://blackmarble.gsfc.nasa.gov/>) and ~~detailed~~ urban land cover data can ~~not only support support not only~~ the development of emission inventories but also sector-orientated ~~investigations with mapped atmospheric concentrations evaluations with atmospheric observations~~ of CO₂ and co-emitted pollutants ~~from space~~. This work demonstrates the benefit of using high-resolution urban land cover ~~datasets like WUDAPT in informing classifications to provide independent information about~~ locations of various anthropogenic activities, building
725 structures, and vegetation coverage. ~~Yet, such high-resolution urban datasets (like WUDAPT and NLCD) are currently only available for a limited number of cities across the globe.~~

5 Conclusion

We investigated fossil fuel combustion efficiency by quantifying the emission ratio of CO and CO₂ across Los Angeles, Shanghai, Baotou, and Zibo (Zouping), using nearly coincident observations of TROPOMI XCO and OCO-2/3 XCO₂. ~~The multiple~~
730 Multiple swaths of observations collected by OCO-3 SAMs cover a much broader area relative to OCO-2 swaths, facilitating the determination of background values and the separation of emission signals from different parts of a city. We incorporate spatial gradients in ~~the~~ background values by calculating the background ~~for each per~~ swath and correcting for the urban-background gradient due to non-anthropogenic sources and sinks. Sensor-specific averaging kernel profiles and meteorological conditions

were accounted for using an atmospheric transport model (X-STILT). The ratio between XCO and XCO₂ enhancements with-
 735 out considering such sensor-specific factors is normally lower than the emission ratio. Cases with severe asynchronicity, specif-
 ically overpass time differences over 3 hours, ~~are excluded from the final result. Temporal variations in the wind fields may
 result in different source regions with respect to the satellite soundings. Therefore, properly correspond to significant changes
 in urban plumes. Properly~~ accounting for the ~~meteorology or the overpass-specific meteorological condition or~~ source-receptor
~~relation and identifying the soundings affected by the relationship and identifying only the soundings influenced by~~ urban emis-
 740 sions is ~~important~~critical for estimating ER for cities, which is ~~the main reason that realized using~~ an atmospheric transport
 modelis-. ~~Such model approach is then~~ used to identify soundings strongly affected by heavy industry.

~~The~~ As a result, the overall city-level ER_{CO} for Shanghai (~~10.5~~10.2±0.4 mmol mol⁻¹) is slightly larger than ~~the city-level
 that~~ for Los Angeles (~~9.79~~9.6±0.5 mmol mol⁻¹). ~~Looking at the sub-city scale, industry-related~~Industry-related ER_{CO} for
 Shanghai are much larger than ~~the its~~ city-level ~~for Shanghai average~~; whereas industry-related ER_{CO} ~~for LA are~~ slightly lower
 745 than ~~the its~~ city-level ~~for LA. This divergence in ERs is likely driven by the distinct industrial processes between the two
 megacities. ERs average.~~ ERs tied to heavy industry regions in Shanghai (~~18.4~~18.8 mmol mol⁻¹) are approximately equal
 to the city-level ER_{CO} for the industry-orientated city of Baotou (~~18.4~~17.3±~~0.6~~0.5 mmol mol⁻¹). High ERs highlight the
 poor ~~burning combustion~~ efficiency tied to ~~certain~~ industrial activities, e.g., ~~high CO emissions from metal production~~metal
 productions (Table 1).

750 With future satellites (e.g., GeoCarb, TEMPO, CO2M) providing better spatial and temporal coverage of XCO₂, ~~XCO, and
 other and~~ relevant co-located ~~tracer~~ observations, it ~~may will~~ be possible to monitor and verify temporal trend ~~or variations in
 combustion efficiencies for and variation in the combustion efficiency over~~ hotspots within an urban area, which ~~has significant
 implications will provide significant guidance~~ for urban planning and emission control.

Code and data availability. OCO-3 L2 B10r XCO₂ data and TROPOMI XCO data were accessed from <https://doi.org/10.22002/D1.2046>
 755 and [10.5270/S5P-1hkp7rp](https://doi.org/10.5270/S5P-1hkp7rp), respectively. X-STILT code has been modified to work with TROPOMI data archived on github branch at
<https://github.com/uataq/X-STILT>. We kindly ask the users to follow the code policy in utilizing and acknowledging the X-STILT code
 for interpreting TROPOMI column data. Hourly NEE fluxes from SMUrF are archived on Oak Ridge National Lab DAAC at
<https://doi.org/10.3334/ORNLDAAC/1899>.

Appendix A: List of prior studies collected in Figure 1

Sector in Fig. 1a	Location	Years	Reference	Additional notes
Traffic	Denver, US	1997	Bradley et al. (2000)	
Traffic	Switzerland	2004	Vollmer et al. (2007), Table 2	Gubrist Tunnel
Traffic	CONUS	2005-2007	Bishop and Siedman (2008)	Chicago, Denver, Los Angeles, Phoenix
Traffic	Paris	2012	Ammoura et al. (2014), Table 2	Tunnel (congestion vs. moving)
Traffic	Switzerland	2011	Popa et al. (2014), Table 1	Isisberg Tunnel (moving)
Traffic	Beijing, China	2007	Westerdahl et al. (2009)	diesel heavy-duty vs. gasoline light-duty
Shipping	China	2011	Zhang et al. (2016), Table 3	Diesel engines; Estimated from EFs
Shipping	Western Europe	2007	Moldanová et al. (2009), Table 5	Diesel engine; Estimated from EFs
Shipping	Texas	2006	Williams et al. (2009), Figure 2	Diesel engines; Estimated from EFs
Shipping	Global	NA	Akagi et al. (2011), Table 1-2	Estimated from EFs
<small>highBIOfuel+FF-SE-Ann-2007-Liu et al. (2010); Table 2 BIOfuel+FF-Ann-2009-Russo et al. (2003); Table 9 Central, Coastal, SE and WSW-Ann Biomass burning</small>				

760

Urban areas in Fig. 1b	Observation years	Reference
Los Angeles (LA)	2002 and 2010	Brioude et al. (2013)
LA	2007-2008	Djuricin et al. (2010)
LA	2008 and 2010	Wennberg et al. (2012)
LA	2010	Silva et al. (2013); Silva and Arellano (2017)
LA	2013-2016	Hedelius et al. (2016)
LA	2019-2021	This study , Figure 7
Pasadena	2007	Wennberg et al. (2012), Table 2
Sacramento	2009	Turnbull et al. (2011a), Sect. 3.2
Indianapolis (Indy)	2012-2014	Turnbull et al. (2015)
Salt Lake City (SLC)	2015-2016	Bares et al. (2018), Table 2
Edinburgh	2005	Famulari et al. (2010), Table 1
Paris	2010	Lopez et al. (2013)
Paris	2010-2014	Ammoura et al. (2016), Table 1
London	2006	Harrison et al. (2012), Figure 27
London	2012	O'Shea et al. (2014), Table 3
London	2016	Pitt et al. (2019), Table 2
Rotterdam	2011	Super et al. (2017)
Germany Alps	2012-2013	Ghasemifard et al. (2019)
Hungary	2017	Haszpra et al. (2019), Table 1
St. Petersburg	2019	Makarova et al. (2021)
Miyun	2004-2008	Wang et al. (2010), Table 2
Beijing	2006	Han et al. (2009), Figure 11
Shangdianzi	2009-2010	Turnbull et al. (2011b)
Nanjing	2011	Huang et al. (2015), Sect. 3.4.2
Seoul	2016	Tang et al. (2018), Table 3
Seoul	2019	Sim et al. (2020), Table 2
Jingdezhen	2017-2018	Xia et al. (2020), Table 3
Zibo, Baotou, Shanghai	2019-2021	This study , Figures 6-7

Author contributions. DW designed and carried out this analysis. JL, POW, and PIP supervised this study. RRN, MK, and AE provided the bias-corrected B10 data for OCO-3 SAMs used in this work. All authors participated in the interpretation of the results and paper writing plus editing.

765 *Competing interests.* The authors declare no conflict of interests.

Acknowledgements. The production of the OCO-3 science data products used in this paper was carried out at the Jet Propulsion Laboratory, California Institute of Technology, under a contract with the National Aeronautics and Space Administration [prime contract num-

ber 80NM0018D0004]. The research effort was funded by the Jet Propulsion Laboratory Research and Technology Development project R.21.023.106. The analysis is supported by the W.M. Keck Institute for Space Studies and by the National Aeronautics and Space Administration (grant number 80NSSC21k1064). The computations presented here were conducted in the Resnick High Performance Computing Center, a facility supported by Resnick Sustainability Institute at the California Institute of Technology. The first author appreciates the discussion with Joshua Laughner, Eric Kort, Tomohiro Oda, and John Lin. [We thank Julia Marshall and the second anonymous referee for their careful read of our submitted manuscript and for their constructive suggestions that have helped improve our study.](#)

References

- 775 Akagi, S., Yokelson, R. J., Wiedinmyer, C., Alvarado, M., Reid, J., Karl, T., Crouse, J., and Wennberg, P.: Emission factors for open and domestic biomass burning for use in atmospheric models, *Atmospheric Chemistry and Physics*, 11, 4039–4072, 2011.
- Ammoura, L., Xueref-Remy, I., Gros, V., Baudic, A., Bonsang, B., Petit, J. E., Perrussel, O., Bonnaire, N., Sciare, J., and Chevallier, F.: Atmospheric measurements of ratios between CO₂ and co-emitted species from traffic: A tunnel study in the Paris megacity, *Atmospheric Chemistry and Physics*, 14, 12 871–12 882, <https://doi.org/10.5194/acp-14-12871-2014>, 2014.
- 780 Ammoura, L., Xueref-Remy, I., Vogel, F., Gros, V., Baudic, A., Bonsang, B., Delmotte, M., Té, Y., and Chevallier, F.: Exploiting stagnant conditions to derive robust emission ratio estimates for CO₂, CO and volatile organic compounds in Paris, *Atmospheric Chemistry and Physics*, 16, 15 653–15 664, <https://doi.org/10.5194/acp-16-15653-2016>, 2016.
- Bares, R., Lin, J. C., Hoch, S. W., Baasandorj, M., Mendoza, D. L., Fasoli, B., Mitchell, L., and Stephens, B. B.: The wintertime covariation of CO₂ and criteria pollutants in an urban valley of the Western United States, *Journal of Geophysical Research: Atmospheres*, 123, 2684–2703, 2018.
- 785 Bishop, G. A. and Stedman, D. H.: A decade of on-road emissions measurements, *Environmental Science & Technology*, 42, 1651–1656, 2008.
- Bradley, K. S., Brooks, K. B., Hubbard, L. K., Popp, P. J., and Stedman, D. H.: Motor vehicle fleet emissions by OP-FTIR, *Environmental Science and Technology*, 34, 897–899, <https://doi.org/10.1021/es9909226>, 2000.
- 790 Brioude, J., Kim, S. W., Angevine, W. M., Frost, G. J., Lee, S. H., McKeen, S. A., Trainer, M., Fehsenfeld, F. C., Holloway, J. S., Ryerson, T. B., Williams, E. J., Petron, G., and Fast, J. D.: Top-down estimate of anthropogenic emission inventories and their interannual variability in Houston using a mesoscale inverse modeling technique, *Journal of Geophysical Research Atmospheres*, 116, <https://doi.org/10.1029/2011JD016215>, 2011.
- Brioude, J., Petron, G., Frost, G. J., Ahmadov, R., Angevine, W. M., Hsie, E. Y., Kim, S. W., Lee, S. H., McKeen, S. A., Trainer, M., Fehsenfeld, F. C., Holloway, J. S., Peischl, J., Ryerson, T. B., and Gurney, K. R.: A new inversion method to calculate emission inventories without a prior at mesoscale: Application to the anthropogenic CO₂ emission from Houston, Texas, *Journal of Geophysical Research Atmospheres*, 117, <https://doi.org/10.1029/2011JD016918>, 2012.
- 795 Brioude, J., Angevine, W. M., Ahmadov, R., Kim, S. W., Evan, S., McKeen, S. A., Hsie, E. Y., Frost, G. J., Neuman, J. A., Pollack, I. B., Peischl, J., Ryerson, T. B., Holloway, J., Brown, S. S., Nowak, J. B., Roberts, J. M., Wofsy, S. C., Santoni, G. W., Oda, T., and Trainer, M.: Top-down estimate of surface flux in the Los Angeles Basin using a mesoscale inverse modeling technique: Assessing anthropogenic emissions of CO, NO_x and CO₂ and their impacts, *Atmospheric Chemistry and Physics*, 13, 3661–3677, <https://doi.org/10.5194/acp-13-3661-2013>, 2013.
- [Chance, K., Liu, X., Suleiman, R., Abad, G. G., Zoogman, P., Wang, H., Nowlan, C., Huang, G., Sun, K., Al-Saadi, J., et al.: TEMPO Green Paper: Chemistry experiments with the Tropospheric Emissions: Monitoring of Pollution instrument, 2022.](#)
- 800 Chandra, N., Lal, S., Venkataramani, S., Patra, P. K., and Sheel, V.: Temporal variations of atmospheric CO₂ and CO at Ahmedabad in western India, *Atmospheric Chemistry and Physics*, 16, 6153–6173, <https://doi.org/10.5194/acp-16-6153-2016>, 2016.
- Ching, J., Mills, G., Bechtel, B., See, L., Feddema, J., Wang, X., Ren, C., Brousse, O., Martilli, A., Neophytou, M., et al.: WUDAPT: An urban weather, climate, and environmental modeling infrastructure for the anthropocene, *Bulletin of the American Meteorological Society*, 99, 1907–1924, 2018.

- 810 Crisp, D., Fisher, B., O'Dell, C., Frankenberg, C., Basilio, R., Bösch, H., Brown, L., Castano, R., Connor, B., Deutscher, N., et al.: The ACOS CO₂ retrieval algorithm—Part II: Global X CO₂ data characterization, *Atmospheric Measurement Techniques*, 5, 687–707, 2012.
~~Ezader, B. H., Byun~~
~~Crouse, J., DeCarlo, P., Blake, D. W., Kim, S.-T., and Carter, W. P.: A study of VOC reactivity in the Houston-Galveston air mixture utilizing an extended version of SAPRC-99 chemical mechanism, *Atmospheric Environment*, R., Emmons, L., Campos, T., Apel, E.,~~
- 815 ~~Clarke, A., Weinheimer, A., McCabe, D., Yokelson, R. J., et al.: Biomass burning and urban air pollution over the Central Mexican Plateau, *Atmospheric Chemistry and Physics*, 9, 42, 5733–5742, 2008. 4929–4944, 2009.~~
~~de Foy, B.: City-level variations in NO_x emissions derived from hourly monitoring data in Chicago, *Atmospheric Environment*, 176, 128–139, 2018.~~
- Demetillo, M. A. G., Harkins, C., McDonald, B. C., Chodrow, P. S., Sun, K., and Pusede, S. E.: Space-Based Observational Constraints on
820 NO₂ Air Pollution Inequality From Diesel Traffic in Major US Cities, *Geophysical Research Letters*, 48, e2021GL094333, 2021.
~~Demuzere, M., Kittner, J., Martilli, A., Mills, G., Moede, C., Stewart, I. D., van Vliet, J., and Bechtel, B.: A global map of Local Climate Zones to support earth system modelling and urban scale environmental science, *Earth System Science Data Discussions*, pp. 1–57, 2022.~~
- Djuricin, S., Pataki, D. E., and Xu, X.: A comparison of tracer methods for quantifying CO₂ sources in an urban region, *Journal of Geophys-*
825 *ical Research Atmospheres*, 115, <https://doi.org/10.1029/2009JD012236>, 2010.
- Duncan, B. N., Lamsal, L. N., Thompson, A. M., Yoshida, Y., Lu, Z., Streets, D. G., Hurwitz, M. M., and Pickering, K. E.: A space-based, high-resolution view of notable changes in urban NO_x pollution around the world (2005–2014), *Journal of Geophysical Research: Atmospheres*, 121, 976–996, 2016.
- Eldering, A.: OCO-3 B10 QTS Evaluation XCO₂ Lite Files, <https://doi.org/10.22002/D1.2046>, 2021.
- 830 Eldering, A., Taylor, T. E., O'Dell, C. W., and Pavlick, R.: The OCO-3 mission: measurement objectives and expected performance based on 1 year of simulated data, *Atmospheric Measurement Techniques*, 12, 2341–2370, 2019.
- Famulari, D., Nemitz, E., Di Marco, C., Phillips, G. J., Thomas, R., House, E., and Fowler, D.: Eddy-covariance measurements of nitrous oxide fluxes above a city, *Agricultural and forest meteorology*, 150, 786–793, 2010.
- Fasoli, B., Lin, J. C., Bowling, D. R., Mitchell, L., and Mendoza, D.: Simulating atmospheric tracer concentrations for spatially distributed
835 receptors: updates to the Stochastic Time-Inverted Lagrangian Transport model's R interface (STILT-R version 2), *Geoscientific Model Development*, 11, 2813–2824, 2018.
- Fujinawa, T., Kuze, A., Suto, H., Shiomi, K., Kanaya, Y., Kawashima, T., Kataoka, F., Mori, S., Eskes, H., and Tanimoto, H.: First concurrent observations of NO₂ and CO₂ from power plant plumes by airborne remote sensing, *Geophysical Research Letters*, 48, e2021GL092685, 2021.
- 840 Ghasemifard, H., Vogel, F. R., Yuan, Y., Luepke, M., Chen, J., Ries, L., Leuchner, M., Schunk, C., Noreen Vardag, S., and Menzel, A.: Pollution events at the high-altitude mountain site Zugspitze-Schneefernerhaus (2670 m asl), Germany, *Atmosphere*, 10, 330, 2019.
- ~~Gonzalez, A., Millet, D. B., Yu, X., Wells, K. C., Griffis, T. J., Baier, B. C., Campbell, P. C., Choi, Y., DiGangi, J. P., Gvakharia, A., et al.: Fossil Versus Nonfossil CO Sources in the US: New Airborne Constraints From ACT-America and GEM, *Geophysical Research Letters*, 48, e2021GL093361, 2021.~~
- 845 Gurney, K. R., Patarasuk, R., Liang, J., Song, Y., O'Keefe, D., Rao, P., Whetstone, J. R., Duren, R. M., Eldering, A., and Miller, C.: The Hestia fossil fuel CO₂ emissions data product for the Los Angeles megacity (Hestia-LA), *Earth System Science Data*, 11, 1309–1335, <https://doi.org/10.5194/essd-11-1309-2019>, 2019.

- Hakkarainen, J., Szlag, M. E., Ialongo, I., Retscher, C., Oda, T., and Crisp, D.: Analyzing nitrogen oxides to carbon dioxide emission ratios from space: A case study of Matimba Power Station in South Africa, *Atmospheric Environment: X*, p. 100110, <https://doi.org/10.1016/j.aeaoa.2021.100110>, 2021.
- Han, S., Kondo, Y., Oshima, N., Takegawa, N., Miyazaki, Y., Hu, M., Lin, P., Deng, Z., Zhao, Y., Sugimoto, N., et al.: Temporal variations of elemental carbon in Beijing, *Journal of Geophysical Research: Atmospheres*, 114, 2009.
- Harrison, R. M., Dall'Osto, M., Beddows, D., Thorpe, A. J., Bloss, W. J., Allan, J. D., Coe, H., Dorsey, J. R., Gallagher, M., Martin, C., et al.: Atmospheric chemistry and physics in the atmosphere of a developed megacity (London): an overview of the REPARTEE experiment and its conclusions, *Atmospheric Chemistry and Physics*, 12, 3065–3114, 2012.
- Haszpra, L., Ferenczi, Z., and Barcza, Z.: Estimation of greenhouse gas emission factors based on observed covariance of CO₂, CH₄, N₂O and CO mole fractions, *Environmental Sciences Europe*, 31, <https://doi.org/10.1186/s12302-019-0277-y>, 2019.
- Hedelius, J. K., Viatte, C., Wunch, D., Roehl, C. M., Toon, G. C., Chen, J., Jones, T., Wofsy, S. C., Franklin, J. E., Parker, H., Dubey, M. K., and Wennberg, P. O.: Assessment of errors and biases in retrievals of XCO₂, XCH₄, XCO, and XN₂O from a 0.5 cm⁻¹ resolution solar-viewing spectrometer, *Atmospheric Measurement Techniques*, 9, 3527–3546, <https://doi.org/10.5194/amt-9-3527-2016>, 2016.
- Hedelius, J. K., Liu, J., Oda, T., Maksyutov, S., Roehl, C. M., Iraci, L. T., Podolske, J. R., Hillyard, P. W., Liang, J., Gurney, K. R., Wunch, D., and Wennberg, P. O.: Southern California megacity CO₂, CH₄, and CO flux estimates using ground-and space-based remote sensing and a Lagrangian model, *Atmospheric Chemistry and Physics*, 18, 16 271–16 291, <https://doi.org/10.5194/acp-18-16271-2018>, 2018.
- Huang, X., Wang, T., Talbot, R., Xie, M., Mao, H., Li, S., Zhuang, B., Yang, X., Fu, C., Zhu, J., et al.: Temporal characteristics of atmospheric CO₂ in urban Nanjing, China, *Atmospheric Research*, 153, 437–450, 2015.
- [Hudman, R. C., Murray, L. T., Jacob, D. J., Millet, D., Turquety, S., Wu, S., Blake, D., Goldstein, A., Holloway, J., and Sachse, G. W.: Biogenic versus anthropogenic sources of CO in the United States, *Geophysical Research Letters*, 35, 2008.](#)
- Kaiser, J., Heil, A., Andreae, M., Benedetti, A., Chubarova, N., Jones, L., Morcrette, J.-J., Razinger, M., Schultz, M., Suttie, M., et al.: Biomass burning emissions estimated with a global fire assimilation system based on observed fire radiative power, *Biogeosciences*, 9, 527–554, 2012.
- Kerr, G. H., Goldberg, D. L., and Anenberg, S. C.: COVID-19 pandemic reveals persistent disparities in nitrogen dioxide pollution, *Proceedings of the National Academy of Sciences*, 118, 2021.
- Kiel, M., Eldering, A., Roten, D. D., Lin, J. C., Feng, S., Lei, R., Lauvaux, T., Oda, T., Roehl, C. M., Blavier, J.-F., et al.: Urban-focused satellite CO₂ observations from the Orbiting Carbon Observatory-3: A first look at the Los Angeles megacity, *Remote Sensing of Environment*, 258, 112 314, 2021.
- [~~Lai, S., Baker, A., Schuck, T., Velthoven, P. v., Oram, D., Zahn, A., Hermann, M., Weigelt, A., Slemr, F., Brenninkmeijer, C., et al.: Pollution events observed during CARIBIC flights in the upper troposphere between South China and the Philippines, *Atmospheric Chemistry and Physics*, 10, 1649–1660, 2010.~~](#)
- Lama, S., Houweling, S., Boersma, K. F., Eskes, H., Aben, I., Gon, H. A. C. D. V. D., Krol, M. C., Dolman, H., Borsdorff, T., and Lorente, A.: Quantifying burning efficiency in megacities using the NO₂:CO ratio from the Tropospheric Monitoring Instrument (TROPOMI), *Atmospheric Chemistry and Physics*, 20, 10 295–10 310, <https://doi.org/10.5194/acp-20-10295-2020>, 2020.
- Laughner, J. L., Neu, J. L., Schimel, D., Wennberg, P. O., Barsanti, K., Bowman, K. W., Chatterjee, A., Croes, B. E., Fitzmaurice, H. L., Henze, D. K., et al.: Societal shifts due to COVID-19 reveal large-scale complexities and feedbacks between atmospheric chemistry and climate change, *Proceedings of the National Academy of Sciences*, 118, 2021.

- 885 Lei, R., Feng, S., Danjou, A., Broquet, G., Wu, D., Lin, J. C., O'Dell, C. W., and Lauvaux, T.: Fossil fuel CO₂ emissions over metropolitan areas from space: A multi-model analysis of OCO-2 data over Lahore, Pakistan, *Remote Sensing of Environment*, 264, 112 625, 2021.
- Lin, J. and Gerbig, C.: Accounting for the effect of transport errors on tracer inversions, *Geophysical Research Letters*, 32, 2005.
- Lin, J., Gerbig, C., Wofsy, S., Andrews, A., Daube, B., Davis, K., and Grainger, C.: A near-field tool for simulating the upstream influence of atmospheric observations: The Stochastic Time-Inverted Lagrangian Transport (STILT) model, *Journal of Geophysical Research: Atmospheres*, 108, 2003.
- 890 Lin, J. C., Mitchell, L., Crosman, E., Mendoza, D. L., Buchert, M., Bares, R., Fasoli, B., Bowling, D. R., Pataki, D., Catharine, D., Strong, C., Gurney, K. R., Patarasuk, R., Baasandorj, M., Jacques, A., Hoch, S., Horel, J., and Ehleringer, J.: CO₂ and carbon emissions from cities linkages to air quality, socioeconomic activity, and stakeholders in the Salt Lake city urban area, *Bulletin of the American Meteorological Society*, 99, 2325–2339, <https://doi.org/10.1175/BAMS-D-17-0037.1>, 2018.
- 895 Lin, J. C., Bares, R., Fasoli, B., Garcia, M., Crosman, E., and Lyman, S.: Declining methane emissions and steady, high leakage rates observed over multiple years in a western US oil/gas production basin, *Scientific reports*, 11, 1–12, 2021.
- Lindenmaier, R., Dubey, M. K., Henderson, B. G., Butterfield, Z. T., Herman, J. R., Rahn, T., and Lee, S. H.: Multiscale observations of CO₂, ¹³CO₂, and pollutants at Four Corners for emission verification and attribution, *Proceedings of the National Academy of Sciences of the United States of America*, 111, 8386–8391, <https://doi.org/10.1073/pnas.1321883111>, 2014.
- 900 Lopez, M., Schmidt, M., Delmotte, M., Colomb, A., Gros, V., Janssen, C., Lehman, S. J., Mondelain, D., Perrussel, O., Ramonet, M., Xueref-Remy, I., and Bousquet, P.: CO, NO_x and 13CO₂ as tracers for fossil fuel CO₂: Results from a pilot study in Paris during winter 2010, *Atmospheric Chemistry and Physics*, 13, 7343–7358, <https://doi.org/10.5194/acp-13-7343-2013>, 2013.
- Makarova, M. V., Alberti, C., Ionov, D. V., Hase, F., Foka, S. C., Blumenstock, T., Warneke, T., Virolainen, Y. A., Kostsov, V. S., Frey, M., Poberovskii, A. V., Timofeyev, Y. M., Paramonova, N. N., Volkova, K. A., Zaitsev, N. A., Biryukov, E. Y., Osipov, S. I., Makarov, B. K., Polyakov, A. V., Ivakhov, V. M., Imhasin, H. K., and Mikhailov, E. F.: Emission Monitoring Mobile Experiment (EMME): An overview and first results of the St. Petersburg megacity campaign 2019, *Atmospheric Measurement Techniques*, 14, 1047–1073, <https://doi.org/10.5194/amt-14-1047-2021>, 2021.
- 905 Miller, S. M., Matross, D. M., Andrews, A. E., Millet, D. B., Longo, M., Gottlieb, E. W., Hirsch, A. I., Gerbig, C., Lin, J. C., Daube, B. C., et al.: Sources of carbon monoxide and formaldehyde in North America determined from high-resolution atmospheric data, *Atmospheric Chemistry and Physics*, 8, 7673–7696, 2008.
- 910 Mitchell, L. E., Lin, J. C., Bowling, D. R., Pataki, D. E., Strong, C., Schauer, A. J., Bares, R., Bush, S. E., Stephens, B. B., Mendoza, D., et al.: Long-term urban carbon dioxide observations reveal spatial and temporal dynamics related to urban characteristics and growth, *Proceedings of the National Academy of Sciences*, 115, 2912–2917, 2018.
- Moldanová, J., Fridell, E., Popovicheva, O., Demirdjian, B., Tishkova, V., Faccineto, A., and Focsa, C.: Characterisation of particulate matter and gaseous emissions from a large ship diesel engine, *Atmospheric Environment*, 43, 2632–2641, 2009.
- 915 Nathan, B., Lauvaux, T., Turnbull, J., and Gurney, K.: Investigations into the use of multi-species measurements for source apportionment of the Indianapolis fossil fuel CO₂ signal, *Elementa*, 6, <https://doi.org/10.1525/elementa.131>, 2018.
- O'Shea, S. J., Allen, G., Fleming, Z. L., Bauguitte, S. J.-B., Percival, C. J., Gallagher, M. W., Lee, J., Helfter, C., and Nemitz, E.: Area fluxes of carbon dioxide, methane, and carbon monoxide derived from airborne measurements around Greater London: A case study during summer 2012, *Journal of Geophysical Research: Atmospheres*, 119, 4940–4952, 2014.
- 920

- Palmer, P. I., Suntharalingam, P., Jones, D. B., Jacob, D. J., Streets, D. G., Fu, Q., Vay, S. A., and Sachse, G. W.: Using CO₂ : CO correlations to improve inverse analyses of carbon fluxes, *Journal of Geophysical Research Atmospheres*, 111, <https://doi.org/10.1029/2005JD006697>, 2006.
- 925 Park, H., Jeong, S., Park, H., Labzovskii, L. D., and Bowman, K. W.: An assessment of emission characteristics of Northern Hemisphere cities using spaceborne observations of CO₂, CO, and NO₂, *Remote Sensing of Environment*, 254, <https://doi.org/10.1016/j.rse.2020.112246>, 2021.
- Pitt, J. R., Allen, G., Bauguitte, S. J.-B., Gallagher, M. W., Lee, J. D., Drysdale, W., Nelson, B., Manning, A. J., and Palmer, P. I.: Assessing London CO₂, CH₄ and CO emissions using aircraft measurements and dispersion modelling, *Atmospheric Chemistry and Physics*, 19, 8931–8945, 2019.
- 930 Plant, G., Kort, E. A., Floerchinger, C., Gvakharia, A., Vimont, I., and Sweeney, C.: Large fugitive methane emissions from urban centers along the US East Coast, *Geophysical research letters*, 46, 8500–8507, 2019.
- Popa, M. E., Vollmer, M. K., Jordan, A., Brand, W. A., Pathirana, S. L., Rothe, M., and Röckmann, T.: Vehicle emissions of greenhouse gases and related tracers from a tunnel study: CO : CO₂, N₂O : CH₄ : O₂ : Atios, and the stable isotopes ¹³C and ¹⁸O in CO₂ and CO, *Atmospheric Chemistry and Physics*, 14, 2105–2123, <https://doi.org/10.5194/acp-14-2105-2014>, 2014.
- 935 Reuter, M., Buchwitz, M., Schneising, O., Krautwurst, S., O'Dell, C. W., Richter, A., Bovensmann, H., and Burrows, J. P.: Towards monitoring localized CO₂ emissions from space: Co-located regional CO₂ and NO₂ enhancements observed by the OCO-2 and S5P satellites, *Atmospheric Chemistry and Physics*, 19, 9371–9383, <https://doi.org/10.5194/acp-19-9371-2019>, 2019.
- ~~Russo, R., Talbot, R., Dibb, J. E., Scheuer, E., Seid, G.~~
- ~~Schneising, O., Buchwitz, M., Reuter, M., Jordan, C., Fuelberg, H., Sachse, Bovensmann, H., Burrows, J. P., Borsdorff, T., Deutscher, N. M., Feist, D. G., Avery, M., Vay, S, Griffith, D. W., Hase, F., et al.: Chemical composition of Asian continental outflow over the western Pacific: Results from Transport and Chemical Evolution over the Pacific (TRACE-P), *Journal of Geophysical Research: Atmospheres*, 108, 2003. A scientific algorithm to simultaneously retrieve carbon monoxide and methane from TROPOMI onboard Sentinel-5 Precursor, *Atmospheric Measurement Techniques*, 12, 6771–6802, 2019.~~
- 940 ~~Feist, D. G., Avery, M., Vay, S, Griffith, D. W., Hase, F., et al.: Chemical composition of Asian continental outflow over the western Pacific: Results from Transport and Chemical Evolution over the Pacific (TRACE-P), *Journal of Geophysical Research: Atmospheres*, 108, 2003. A scientific algorithm to simultaneously retrieve carbon monoxide and methane from TROPOMI onboard Sentinel-5 Precursor, *Atmospheric Measurement Techniques*, 12, 6771–6802, 2019.~~
- Schuh, A. E., Otte, M., Lauvaux, T., and Oda, T.: Far-field biogenic and anthropogenic emissions as a dominant source of variability in local urban carbon budgets: A global high-resolution model study with implications for satellite remote sensing, *Remote Sensing of Environment*, 262, 112 473, 2021.
- 945 Schuh, A. E., Otte, M., Lauvaux, T., and Oda, T.: Far-field biogenic and anthropogenic emissions as a dominant source of variability in local urban carbon budgets: A global high-resolution model study with implications for satellite remote sensing, *Remote Sensing of Environment*, 262, 112 473, 2021.
- Shekhar, A., Chen, J., Paetzold, J. C., Dietrich, F., Zhao, X., Bhattacharjee, S., Ruisinger, V., and Wofsy, S. C.: Anthropogenic CO₂ emissions assessment of Nile Delta using XCO₂ and SIF data from OCO-2 satellite, *Environmental Research Letters*, 15, 095 010, 2020.
- Silva, S. and Arellano, A.: Characterizing Regional-Scale Combustion Using Satellite Retrievals of CO, NO₂ and CO₂, *Remote Sensing*, 9, 744, <https://doi.org/10.3390/rs9070744>, 2017.
- 950 Silva, S. J., Arellano, A. F., and Worden, H. M.: Toward anthropogenic combustion emission constraints from space-based analysis of urban CO₂ /CO sensitivity, *Geophysical Research Letters*, 40, 4971–4976, <https://doi.org/10.1002/grl.50954>, 2013.
- Sim, S., Jeong, S., Park, H., Park, C., Kwak, K. H., Lee, S. B., Kim, C. H., Lee, S., Chang, J. S., Kang, H., and Woo, J. H.: Co-benefit potential of urban CO₂ and air quality monitoring: A study on the first mobile campaign and building monitoring experiments in Seoul during the winter, *Atmospheric Pollution Research*, 11, 1963–1970, <https://doi.org/10.1016/j.apr.2020.08.009>, 2020.
- 955 Solazzo, E., Crippa, M., Guizzardi, D., Muntean, M., Choulga, M., and Janssens-Maenhout, G.: Uncertainties in the Emissions Database for Global Atmospheric Research (EDGAR) emission inventory of greenhouse gases, *Atmospheric Chemistry and Physics*, 21, 5655–5683, <https://doi.org/10.5194/acp-21-5655-2021>, 2021.

- Stewart, I. D. and Oke, T. R.: Local climate zones for urban temperature studies, *Bulletin of the American Meteorological Society*, 93, 1879–1900, 2012.
- 960 Super, I., van der Gon, H. A. D., Visschedijk, A. J., Moerman, M. M., Chen, H., van der Molen, M. K., and Peters, W.: Interpreting continuous in-situ observations of carbon dioxide and carbon monoxide in the urban port area of Rotterdam, *Atmospheric Pollution Research*, 8, 174–187, <https://doi.org/10.1016/j.apr.2016.08.008>, 2017.
- Surl, L., Palmer, P. I., and González Abad, G.: Which processes drive observed variations of HCHO columns over India?, *Atmospheric Chemistry and Physics*, 18, 4549–4566, 2018.
- 965 Tang, W., Arellano, A. F., DiGangi, J. P., Choi, Y., Diskin, G. S., Agustí-Panareda, A., Parrington, M., Massart, S., Gaubert, B., Lee, Y., et al.: Evaluating high-resolution forecasts of atmospheric CO and CO₂ from a global prediction system during KORUS-AQ field campaign, *Atmospheric Chemistry and Physics*, 18, 11 007–11 030, 2018.
- Tang, W., Gaubert, B., Emmons, L., Choi, Y., DiGangi, J., Diskin, G., Xu, X., He, C., Worden, H., Tilmes, S., Buchholz, R., Halliday, H., and Arellano, A.: On the relationship between tropospheric CO and CO₂ during KORUS-AQ and its role in constraining anthropogenic CO₂, *Atmospheric Chemistry and Physics*, pp. 1–53, <https://doi.org/10.5194/acp-2020-864>, 2020.
- 970 Taylor, T. E., Eldering, A., Merrelli, A., Kiel, M., Somkuti, P., Cheng, C., Rosenberg, R., Fisher, B., Crisp, D., Basilio, R., et al.: OCO-3 early mission operations and initial (vEarly) XCO₂ and SIF retrievals, *Remote Sensing of Environment*, 251, 112 032, 2020.
- Turnbull, J., Karion, A., Fischer, M., Faloona, I., Guilderson, T., Lehman, S., Miller, B., Miller, J., Montzka, S., Sherwood, T., et al.: Assessment of fossil fuel carbon dioxide and other anthropogenic trace gas emissions from airborne measurements over Sacramento, California in spring 2009, *Atmospheric Chemistry and Physics*, 11, 705–721, 2011a.
- 975 Turnbull, J. C., Tans, P. P., Lehman, S. J., Baker, D., Conway, T. J., Chung, Y. S., Gregg, J., Miller, J. B., Southon, J. R., and Zhou, L. X.: Atmospheric observations of carbon monoxide and fossil fuel CO₂ emissions from East Asia, *Journal of Geophysical Research Atmospheres*, 116, <https://doi.org/10.1029/2011JD016691>, 2011b.
- 980 Turnbull, J. C., Sweeney, C., Karion, A., Newberger, T., Lehman, S. J., Tans, P. P., Davis, K. J., Lauvaux, T., Miles, N. L., Richardson, S. J., et al.: Toward quantification and source sector identification of fossil fuel CO₂ emissions from an urban area: Results from the INFLUX experiment, *Journal of Geophysical Research: Atmospheres*, 120, 292–312, 2015.
- Turner, A. J., Köhler, P., Magney, T. S., Frankenberg, C., Fung, I., and Cohen, R. C.: A double peak in the seasonality of California’s photosynthesis as observed from space, *Biogeosciences*, 17, 405–422, 2020.
- 985 Veefkind, J., Aben, I., McMullan, K., Förster, H., De Vries, J., Otter, G., Claas, J., Eskes, H., De Haan, J., Kleipool, Q., et al.: TROPOMI on the ESA Sentinel-5 Precursor: A GMES mission for global observations of the atmospheric composition for climate, air quality and ozone layer applications, *Remote sensing of environment*, 120, 70–83, 2012.
- Venables, W. N. and Ripley, B. D.: *Modern Applied Statistics with S*, Springer, New York, fourth edn., <http://www.stats.ox.ac.uk/pub/MASS4>, ISBN 0-387-95457-0, 2002.
- 990 Vollmer, M. K., Juergens, N., Steinbacher, M., Reimann, S., Weilenmann, M., and Buchmann, B.: Road vehicle emissions of molecular hydrogen (H₂) from a tunnel study, *Atmospheric Environment*, 41, 8355–8369, 2007.
- Wang, H., Jacob, D. J., Kopacz, M., Jones, D. B. A., Suntharalingam, P., Fisher, J. A., Nassar, R., Pawson, S., and Nielsen, J. E.: Atmospheric Chemistry and Physics Error correlation between CO₂ and CO as constraint for CO₂ flux inversions using satellite data, *Atmos. Chem. Phys.*, 9, 7313–7323, www.atmos-chem-phys.net/9/7313/2009/, 2009.
- 995 Wang, X., Lei, Y., Yan, L., Liu, T., Zhang, Q., and He, K.: A unit-based emission inventory of SO₂, NO_x and PM for the Chinese iron and steel industry from 2010 to 2015, *Science of the total environment*, 676, 18–30, 2019.

- Wang, Y., Munger, J. W., Xu, S., McElroy, M. B., Hao, J., Nielsen, C. P., and Ma, H.: CO₂ and its correlation with CO at a rural site near Beijing: Implications for combustion efficiency in China, *Atmospheric Chemistry and Physics*, 10, 8881–8897, <https://doi.org/10.5194/acp-10-8881-2010>, 2010.
- 1000 Wennberg, P. O., Mui, W., Wunch, D., Kort, E. A., Blake, D. R., Atlas, E. L., Santoni, G. W., Wofsy, S. C., Diskin, G. S., Jeong, S., et al.: On the sources of methane to the Los Angeles atmosphere, *Environmental science & technology*, 46, 9282–9289, 2012.
- [Wannberg, P. O., Wunch, D., Roehl, C., Blavier, J-F, Toon, G. C., and Allen, N.: TCCON data from Caltech \(US\), Release GGG2020R0, TCCON data archive, hosted by CaltechDATA, https://doi.org/10.14291/tcon.ggg2020.pasadena01.R0, 2017.](https://doi.org/10.14291/tcon.ggg2020.pasadena01.R0)
- Westerdahl, D., Wang, X., Pan, X., and Zhang, K. M.: Characterization of on-road vehicle emission factors and microenvironmental air quality in Beijing, China, *Atmospheric Environment*, 43, 697–705, 2009.
- 1005 Williams, E., Lerner, B., Murphy, P., Herndon, S., and Zahniser, M.: Emissions of NO_x, SO₂, CO, and HCHO from commercial marine shipping during Texas Air Quality Study (TexAQS) 2006, *Journal of Geophysical Research: Atmospheres*, 114, 2009.
- Wu, D., Lin, J. C., Fasoli, B., Oda, T., Ye, X., Lauvaux, T., Yang, E. G., and Kort, E. A.: A Lagrangian approach towards extracting signals of urban CO₂ emissions from satellite observations of atmospheric column CO₂ (XCO₂): X-Stochastic Time-Inverted Lagrangian
- 1010 Transport model (“X-STILT v1”), *Geoscientific Model Development*, 11, 4843–4871, 2018.
- Wu, D., Lin, J. C., Oda, T., and Kort, E. A.: Space-based quantification of per capita CO₂ emissions from cities, *Environmental Research Letters*, 15, 035004, 2020.
- Wu, D., Lin, J. C., Duarte, H. F., Yadav, V., Parazoo, N. C., Oda, T., and Kort, E. A.: A model for urban biogenic CO₂ fluxes: Solar-Induced Fluorescence for Modeling Urban biogenic Fluxes (SMUrF v1), *Geoscientific Model Development*, 14, 3633–3661, 2021.
- 1015 Wunch, D., Wennberg, P., Toon, G., Keppel-Aleks, G., and Yavin, Y.: Emissions of greenhouse gases from a North American megacity, *Geophysical research letters*, 36, 2009.
- Xia, L., Zhang, G., Liu, L., Li, B., Zhan, M., Kong, P., and Wang, H.: Atmospheric CO₂ and CO at Jingdezhen station in central China: Understanding the regional transport and combustion efficiency, *Atmospheric Environment*, 222, 117104, 2020.
- Ye, X., Lauvaux, T., Kort, E. A., Oda, T., Feng, S., Lin, J. C., Yang, E. G., and Wu, D.: Constraining Fossil Fuel CO₂ Emissions From Urban
- 1020 Area Using OCO-2 Observations of Total Column CO₂, *Journal of Geophysical Research: Atmospheres*, 125, e2019JD030528, 2020.
- Yokota, T., Yoshida, Y., Eguchi, N., Ota, Y., Tanaka, T., Watanabe, H., and Maksyutov, S.: Global concentrations of CO₂ and CH₄ retrieved from GOSAT: First preliminary results, *Sola*, 5, 160–163, 2009.
- Yuan, L. and Smith, A. C.: CO and CO₂ emissions from spontaneous heating of coal under different ventilation rates, *International Journal of Coal Geology*, 88, 24–30, 2011.
- 1025 Zhang, F., Chen, Y., Tian, C., Lou, D., Li, J., Zhang, G., and Matthias, V.: Emission factors for gaseous and particulate pollutants from offshore diesel engine vessels in China, *Atmospheric Chemistry and Physics*, 16, 6319–6334, 2016.
- [Zhang, Y., Smith, S. J., Bowden, J. H., Adelman, Z., and West, J. J.: Co-benefits of global, domestic, and sectoral greenhouse gas mitigation for US air quality and human health in 2050, Environmental Research Letters, 12, 114033, 2017.](https://doi.org/10.1029/2017GL074033)
- Zhang, Y., Joiner, J., Alemohammad, S. H., Zhou, S., and Gentine, P.: A global spatially contiguous solar-induced fluorescence (CSIF)
- 1030 dataset using neural networks, *Biogeosciences*, 15, 5779–5800, 2018.
- [Zhu, L., Jacob, D. J., Mickley, L. J., Marais, E. A., Cohan, D. S., Yoshida, Y., Duncan, B. N., Abad, G. G., and Chance, K. V.: Anthropogenic emissions of highly reactive volatile organic compounds in eastern Texas inferred from oversampling of satellite \(OMI\) measurements of HCHO columns, Environmental Research Letters, 9, 114004, 2014.](https://doi.org/10.1029/2014GL060444)